A Thermodynamically Consistent Phase Field Model for Gas Transport in Saturated Bentonite Accounting for Initial Stress State

Guanlong Guo[1] · Mamadou Fall[1]

Abstract

A thermodynamically consistent phase field model that accounts for initial stress state is proposed in this paper to simulate the gas migration process in saturated bentonite. The energy contribution due to the fracturing process is included in Coussy's thermodynamic framework for unsaturated porous media. The possible effect of the interfaces between different phases on the driving force functional for phase field and the effective stress has been identified from the proposed thermodynamic framework. In addition, the initial stress state is innovatively accounted for in the phase field model by introducing a fictitious strain tensor that is calculated from its corresponding initial stress tensor. It is the sum of the fictitious strain tensor and the strain tensor due to elastic deformation that governs the evolution of the phase field. The simulated results showed that the effect of the swelling pressure (regarded as the initial effective stress for a high swelling clay) on the fracture initiation has been well described by the proposed method. Specifically, the effect of either isotropic or anisotropic stress state on the fracturing process can be well reflected by the phase field approach based on Rankine-type fracture criterion. In contrast, the phase field approach based on the Griffith fracture criterion is more appropriate for the isotropic stress state than the anisotropic stress state because of the Poisson's effect. Moreover, the gas pressure required to trigger the fracturing process needs to exceed the sum of the porewater pressure and the initial stress. The effect of the boundary condition on the evolution of fluid pressure and total stress has been qualitatively captured. It is found that the boundary with higher stiffness leads to a higher gas pressure in the developed fracture and a higher water pressure and total stress in the surrounding porous matrix. In addition, some key experimental findings, such as the preferential gas flow, the build-up of porewater pressure, the almost fully saturated state and the localized consolidation, have been qualitatively captured by the developed phase field model.

Keywords Phase field · Geological repository · Nuclear waste · Bentonite · Preferential gas flow · Initial stress

✉ Mamadou Fall
mfall@uottawa.ca

[1] Department of Civil Engineering, University of Ottawa, 161 Colonel by, Ottawa, ON K1N 6N5, Canada

1 Introduction

Radioactive wastes generated from nuclear power plants will pose a severe threat to human health and the ecological environment if they cannot be properly dealt with. A widely accepted mitigation method is to deposit the radioactive wastes in a deep geological repository (DGR) that consists of an engineering barrier system (EBS) and a natural barrier system (Ye et al. 2014; Marschall et al. 2005; Rodwell et al. 1999). Bentonite is considered as an ideal buffer material for the EBS because of several desirable properties, such as high adsorptive capacity, low permeability, swelling property and self-sealing ability (Ye et al. 2014; Xu et al. 2015, 2016, 2018; Liu et al. 2015, 2016). However, these properties may be undermined by the transport of gas that is generated from complex physicochemical reactions during the lifespan of a DGR. Four gas transport mechanisms have been identified in previous experimental studies, including advection/diffusion of dissolved gas, visco-capillary two-phase flow, dilatancy-controlled flow (DCF) and macro-fracture flow (Marschall et al. 2005; Fall et al. 2014). The DCF is considered as a dominant mechanism of gas transport in saturated bentonite (Graham et al. 2012; Horseman et al. 1999). Therefore, realistically simulating the DCF is critical to get an in-depth understanding about the gas transport behaviors in saturated bentonite.

DCF is characterized by several complex hydromechanical behaviors, including the development of preferential pathways, the gas breakthrough phenomenon, the volume dilation under constant confining condition (CCC) or the total stress build-up under constant volume condition (CVC), the increase of water pressure and the almost saturated state after gas injection (Graham et al. 2012, 2016; Harrington et al. 2012, 2017, 2019; Daniels and Harrington 2017; Wiseall et al. 2015). It is challenging to fully capture all these behaviors in a single model. Most of previous numerical models focused on reproducing the gas breakthrough phenomenon. Essentially, the gas breakthrough phenomenon results from the rapid growth of preferential pathways under high gas pressure (Graham et al. 2012; Harrington et al. 2019, 2017). To circumvent the explicit simulation of the preferential pathways, the traditional coupled HM model is typically enriched by introducing either damage mechanics, as in Fall et al. (2014), Dagher et al. (2018) and Mahjoub et al. (2017), or plasticity theory, as those in Nguyen and Le (2014); Xu et al. 2013 and Olivella and Alonso (2008). In these models, the gas entry value and the intrinsic permeability are generally expressed as functions of either a damage variable or plastic strain to simulate the rapid changes in these properties. Some empirical parameters are necessary to be introduced to calibrate the simulated gas pressure to fit the experimental data. In contrast, the other characteristics besides the gas breakthrough phenomenon can only be qualitatively described or even missed, as the physical processes during the DCF are rather complicated to be modeled.

Most previous models assumed the bentonite with the developed preferential pathways as a single porosity media. The effect of the preferential pathways on the gas flow behavior is only described by the increase of permeability and the decrease of gas entry value. Thus, the fluid flow in the developed fractures cannot be independently considered. To address this limitation, a double porosity concept was adopted in Guo and Fall (2018) to differentiate the fluid flows in fractures and in pores. Corresponding to the double porosity concept, a double effective stress concept is derived from the mixture theory and the first law of thermodynamics in that paper. Each effective stress controls the evolution of its corresponding porosity. As a result, the opening of the fracture results from the consolidation of porous matrix and the dilation of the whole porous

media. This feature is beneficial to simulating the development of preferential pathways under CVC, which restricts the overall dilation of the specimen. This framework is further improved by considering the damaging effect due to the high gas pressure on the gas transport behaviors, as detailed in Guo and Fall (2020). In this improved model, the independent stress state variables, i.e., net normal stress and suction, rather than the Bishop's-like effective stress, are used to describe the mechanical behaviors of the fractured porous media. This is because the gas pressure fully serves as the pore pressure in the net normal stress, which eases the occurrence of tensile failure. In short, due to the introduction of the double porosity concept, the coupled HM model is more capable of reproducing the experimentally observed behaviors. However, the model is still incapable of explicitly simulating the development of the preferential pathways.

There are several numerical approaches used to explicitly simulate the fracturing process in geomaterials, including the extended finite element method (XFEM) (Mohammadnejad and Khoei 2013a, b; Salimzadeh and Khalili 2015), the finite element method (FEM) enriched by zero thickness interfaces (Nguyen et al. 2017; Carrier and Granet 2012) and the discrete element method (DEM) (Gui et al. 2017; Amarasiri and Kodikara 2011). However, these approaches may be limited to simulating the crack kinking or branching, especially for the three-dimensional case (Miehe et al. 2010a). In contrast, the phase field method presents advantages to model complex fracture topologies, as the fracture initiation, propagation and branching are controlled by a governing equation that can be straightforwardly implemented into the standard FEM. In recent years, the phase field method has been widely used to simulate the hydraulic fracturing in geomaterials, as those in Chen et al. (2020), Zhou et al. (2020), Zhou et al. (2018), Santillán et al. (2018) and Mauthe and Miehe (2017). Then, the hydromechanical-phase field (HM-PF) framework for modeling fracturing in saturated porous media was extended to the unsaturated condition for simulating desiccation cracking (Cajuhi et al. 2018; Heider and Sun 2020). This approach was enriched in Guo and Fall (2019) to simulate the gas-driven fracturing in heterogeneous and saturated bentonite. The proposed framework can well describe the experimentally observed behaviors during gas migration in a qualitative way, such as the preferential gas flow, the build-up of water pressure and total stress and the fully saturated state around the developed fracture. However, the swelling pressure, an important factor controlling the fracturing process, has not yet been considered by the model. Previous experimental studies showed major gas entry occurs when gas pressure reaches the sum of pore water pressure and the swelling pressure (Graham et al. 2012). As stated in Horseman et al. (1999), the effective stress is equivalent to the swelling pressure for a high swelling clay. To address this limitation, the effect of initial stress state on the gas flow behavior will be considered in this paper by introducing a fictitious strain tensor into the phase field method. In addition, a thermodynamically consistent HM-PF framework will be derived from the theory of thermodynamics proposed by Coussy (2004) for unsaturated porous media and the microforce balance law (Gurtin 1996; Choo and Sun 2018a).

This paper is organized as follows: In Sect. 2, the conceptual model for the HM-PF framework and related assumptions are presented. In Sect. 3, governing equations for the stress equilibrium and the microforce balance are derived. The mechanical constitutive models are developed in the framework of Coussy's thermodynamic theory for unsaturated porous media. In Sect. 4, the mass balance equations and constitutive models for hydraulic process are given. The weak form and model implementation are discussed in Sect. 5. The model validation and simulations of gas migration in saturated bentonite are presented in Sect. 6. Finally, conclusions and future works will be given in Sect. 7.

2 Conceptual HM-PF Framework

In this section, a conceptual coupled HM-PF model is proposed based on previous experimental findings and some reasonable assumptions.

2.1 Basic Assumptions

As the copper canister used to seal the radioactive waste is highly resistant to the corrosion of underground water, the buffer material is expected to reach full saturation when the gas is initially generated within the canister. Therefore, the bentonite samples used in most previous gas injection tests were initially saturated. In expansive soils, there may exist three types of pores, i.e., inter-aggregate pores, intra-aggregate pores and interlayer pores, and two types of water, i.e., adsorbed water and capillary water (Gens and Alonso 1992). The ratio of these two types of water plays an important role in controlling the pore structure of the soil (Gens and Alonso 1992, Alonso et al. 1999). In this study, the adsorbed water is assumed as a part of the solid grain for simplicity. Therefore, the saturated expansive soil can be simplified as a normal porous media with a single pore size distribution. This assumption seems reasonable for the current study, as the temperature change and chemical evolution, which may induce significant changes of the adsorbed water, are not considered. In addition, the visco-capillary two-phase flow is assumed to take place in both the pores and the developed fractures.

2.2 Conceptual Model

A conceptual coupled HM-PF model for modeling gas-driven fracturing in saturated bentonite was originally proposed in Guo and Fall (2019). This conceptual model is enriched in this paper. As shown in Fig. 1, the interactive couplings among different fields, including the gas pressure field, p_g, the water pressure field, p_w, the displacement field, $\boldsymbol{u}$, and the phase field, d, are illustrated.

The hydraulic process is characterized by the visco-capillary two-phase flow, and the degree of saturation is controlled by the water retention curve. The hydraulic process influences the mechanical process through the pore pressure that is generally assumed as the
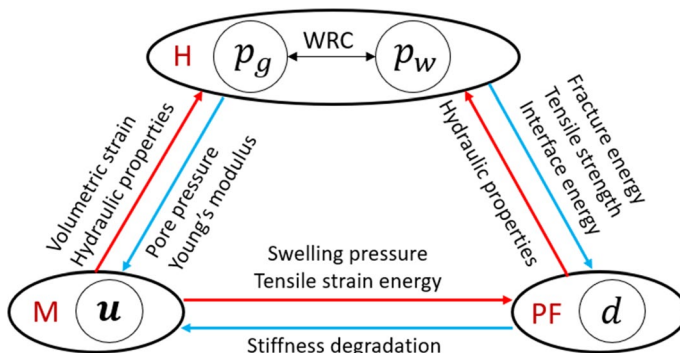
Fig. 1 A conceptual HM-PF model and the associated coupling processes [Modified from (Guo and Fall 2019)]. *Notes* H: Hydraulic process; M: mechanical process; PF: phase field; WRC: water retention curve

average of the gas pressure and water pressure. Alternatively, Coussy (2004) proposed an equivalent pore pressure that considers the contribution from the interfaces between different phases. Meanwhile, the capillary pressure may influence the mechanical properties, such as Young's modulus, fracture energy and tensile strength (Yin and Vanapalli 2018; Qi and Vanapalli 2018). In addition, the free energy of the interfaces may also drive the fracturing process. This coupling will be included in the following thermodynamic framework. However, as it has not yet been validated in experiments, it will not be further discussed in the following simulations.

Conversely, the deformation from the mechanical process changes the storage capability and the mass source of the hydraulic process. In addition, the hydraulic properties, such as gas entry value, intrinsic and relative permeability, are also influenced by the deformation. Meanwhile, the mechanical process also provides the driving force for the fracturing process. In particular, the swelling pressure of the geomaterial, which is considered as an initial stress in the current study, has significant influences on the fracturing process. However, previous phase field models rarely dealt with the effect of initial stress state. Recently, Zhou et al. (2020) proposed a phase field model for hydraulic fracturing that considers the initial stress state. However, it seems that the approach may not be able to differentiate the contribution of different principal components of the initial stress tensor to the fracturing process. To realistically simulate the gas migration behavior, the effect of initial stress state will be further studied in the following part of this paper.

The evolution of the phase field variable represents the fracturing process. The fracture propagation will degrade the mechanical properties, such as the Young's modulus. Meanwhile, the size of the developed fractures is much larger than that of pores in matrix, leading to the increases in relative and intrinsic permeability and the decrease in the gas entry value. The gas, as a result, will preferentially flow through these developed fractures.

The aforementioned coupling processes will be numerically considered in the governing equations and constitutive models for the mechanical and hydraulic process.

3 Mechanical Model

The mechanical process involved in the current topic consists of a microforce system and a macroforce system, as adopted in Na and Sun (2018). The constitutive models for the microforce system and the macroforce system will be derived in a rigorous thermodynamic framework.

3.1 Governing Equations

3.1.1 Macroforce System

Based on the mixture theory and Newton's second law, the momentum balance law for a porous medium (occupying a domain, Ω, bounded by the surface $\partial\Omega$), can be expressed as (Coussy 2004; Borja 2006)

$$\int_{\Omega} \mathbf{b} d\Omega + \int_{\partial\Omega} \mathbf{t} d\partial\Omega = \int_{\Omega} \sum_{\alpha=s,w,g} \left(\rho_\alpha \phi_\alpha \mathbf{a}_\alpha \right) d\Omega \tag{1}$$

where **b** is the body force, **t** is the traction force on the surface, ρ_α is the intrinsic density of phase α, ϕ_α is the volume fraction occupied by phase α, $\mathbf{a}_\alpha$ is the acceleration of phase α, and α denotes s, w and g for solid grain, water and gas, respectively.

As the body force for the porous media only results from the gravity, then

$$\mathbf{b} = \rho\mathbf{g} \tag{2}$$

where $\rho = \sum_{\alpha=s,w,g} \rho_\alpha \phi_\alpha$ is the average density of the porous media and **g** is the gravitational acceleration.

Based on the stress equilibrium on the surface $\partial\Omega$, the traction, **t**, can be expressed with respect to the Cauchy stress tensor as

$$\mathbf{t} = \boldsymbol{\sigma} \cdot \mathbf{n} \tag{3}$$

where $\boldsymbol{\sigma}$ is the total Cauchy stress tensor and $\boldsymbol{n}$ is the outward unit vector normal to the surface.

Substituting Eqs. (2) and (3) into Eq. (1) and applying the Gauss's theorem lead to

$$\int_\Omega \left[\nabla \cdot \boldsymbol{\sigma} + \rho\mathbf{g} - \sum_{\alpha=s,w,g} \left(\rho_\alpha \phi_\alpha \mathbf{a}_\alpha \right) \right] d\Omega = 0 \tag{4}$$

As the integral balance must hold for any arbitrary volume, the integrand in the above equation must be zero. Then, by disregarding the dynamic terms, the strong form for the momentum balance law is derived as

$$\nabla \cdot \boldsymbol{\sigma} + \rho\mathbf{g} = \mathbf{0} \tag{5}$$

3.1.2 Microforce System

The governing equation for phase field is commonly derived from two approaches, i.e., the variational principle of free energy minimization (Chen et al. 2020; Zhou et al. 2018; Santillán et al. 2017) and the microforce balance law (Choo and Sun 2018a, b; Na and Sun 2018; Wilson et al. 2013). The variational principle approach has been adopted to develop the phase field models for simulating hydraulic fracturing in rocks and desiccation cracking in soils, as seen in Mauthe and Miehe (2017), Cajuhi et al. (2018) and Mikelić et al. (2015). In particular, the variational approaches developed in Mauthe and Miehe (2017), Mikelić et al. (2015) incorporated the energy contribution from the fluid into the free energy functional for the saturated porous media. Therefore, these phase field methods for simulating the fracturing process in saturated porous media are more thermodynamically based. As discussed in Sect. 2, the current research topic involves the complex processes, including the multiphase flow, the fluid-driven fracturing and the effect of interfaces. Compared with the variational approach, the microforce balance law approach may be more flexible to account for these complex physical processes during the fracturing process (Choo and Sun 2018a). Thus, the microforce balance law will be adopted in this paper to develop a thermodynamically consistent phase field model to simulate the gas-driven fracturing in initially saturated bentonite.

As done by Gurtin (1996), a set of external microforces, including the surface force, ς, and the body force, γ, the internal microscopic stress, $\boldsymbol{\xi}$, and the internal microscopic body force, π, are introduced to construct the microforce balance law. As given in Gurtin (1996), Wilson et al. (2013), the microforce balance law can be expressed as

$$\int_{\partial\Omega} \varsigma \mathrm{d}\partial\Omega + \int_{\Omega} (\gamma + \pi)\mathrm{d}\Omega = 0 \tag{6}$$

Similar to Eq. (3), the microforce on the surface $\partial\Omega$, i.e., ς, can be expressed as

$$\varsigma = \boldsymbol{\xi} \cdot \mathbf{n} \tag{7}$$

By substituting Eq. (7) into Eq. (6), and neglecting the external microforce, γ, as done in Choo and Sun (2018a), Na and Sun (2018), the microforce balance law can be derived as

$$\int_{\Omega} (\nabla \cdot \boldsymbol{\xi} + \pi)\mathrm{d}\Omega = 0 \tag{8}$$

As the above integral balance holds in any arbitrary volume, the strong form for the microforce balance law can be derived as

$$\nabla \cdot \boldsymbol{\xi} + \pi = 0 \tag{9}$$

3.2 Thermodynamic Analysis

3.2.1 Coussy's Thermodynamic Theory

By using the mixture theory, Coussy (2004) developed a thermodynamically consistent framework for describing the coupled thermo-hydro-mechanical (THM) behaviors of unsaturated porous media. The detailed derivation processes can be found in Coussy (2004). Based on the first law and the second law of thermodynamics, the final form of the Clausius–Duhem inequality is derived as

$$\Phi = \Phi_{\mathrm{int}} + \varphi_f + \varphi_{\mathrm{th}} \geq 0 \tag{10}$$

where Φ_{int} is the dissipation associated with the skeleton (including the solid matrix and the interfaces between different phases), φ_f and φ_{th} are the dissipations associated with the fluid flow and the heat transfer, respectively.

To satisfy the above Clausius–Duhem inequality, a sufficient but unnecessary condition is generally assumed that each dissipation component is nonnegative. As the thermal effect on the hydromechanical process is not considered in the current study, the dissipation related to heat transfer, φ_{th}, will not be discussed in the following. The dissipation due to fluid flow, φ_f, will be discussed in Sect. 4. Here, the dissipation related to the skeleton under isothermal condition can be expressed as (Coussy 2004)

$$\Phi_{\mathrm{int}} = \boldsymbol{\sigma} : \dot{\boldsymbol{\varepsilon}} + p_w \dot{\phi}_w + p_g \dot{\phi}_g - \dot{\Psi}_s \geq 0 \tag{11}$$

where Ψ_s is the skeleton free energy, $\boldsymbol{\varepsilon}$ is the strain tensor, $\phi_w = \phi S_w$ and $\phi_g = \phi S_g$ are volume percentages occupied by water phase and gas phase, respectively, ϕ is porosity and S_w and S_g are degree of saturations for water and gas, respectively.

This thermodynamics framework will be extended to include the contribution from the fracturing process in the following sections.

3.2.2 Clausius–Duhem Inequality

By using the microforce balance law, i.e., Eq. (8), the mechanical power from the micro-force system, P_{mic}, can be derived as (Choo and Sun 2018c)

$$P_{\text{mic}} = \int_{\partial\Omega} (\boldsymbol{\xi} \cdot \mathbf{n})\dot{d}\mathrm{d}\partial\Omega = \int_{\Omega} \left(\boldsymbol{\xi} \cdot \nabla\dot{d} - \pi\dot{d}\right)\mathrm{d}\Omega \tag{12}$$

This mechanical power is then incorporated into the Clausius–Duhem inequality for unsaturated porous media, Eq. (11), to account for the contribution from the fracturing process. This will result in an enriched Clausius–Duhem inequality as:

$$\Phi_{\text{int}} = \boldsymbol{\sigma} : \dot{\boldsymbol{\varepsilon}} + p_w\dot{\phi}_w + p_g\dot{\phi}_g + \boldsymbol{\xi} \cdot \nabla\dot{d} - \pi\dot{d} - \dot{\Psi}_s \geq 0 \tag{13}$$

Reformulating Eq. (13) with respect to suction, i.e., $p_c = p_g - p_w$, yields

$$\Phi_{\text{int}} = \boldsymbol{\sigma} : \dot{\boldsymbol{\varepsilon}} + \overline{p}\dot{\phi} - \phi p_c\dot{S}_w + \boldsymbol{\xi} \cdot \nabla\dot{d} - \pi\dot{d} - \dot{\Psi}_s \geq 0 \tag{14}$$

where $\overline{p} = S_w p_w + \left(1 - S_w\right)p_g$ is the average pore pressure.

In analogy to Coussy (2004), a general form for the skeleton free energy, Ψ_s, that considers the evolution of phase field can be defined as

$$\Psi_s = \psi_s(\boldsymbol{\varepsilon}, d) + \phi U\left(S_w, d\right) \tag{15}$$

where ψ_s is the free energy of solid matrix and U is the free energy of interfaces per unit volume of void space. Note that only elastic strain tensor is considered in the current study.

In previous studies, such as Na and Sun 2018; Wilson et al. 2013, the free energy due to the fracturing process is also included in the free energy of the solid matrix, i.e., ψ_s. This definition may not be appropriate to describe the fracturing as a fully dissipative and irreversible process (Choo and Sun 2018a, b). To remedy this issue, Choo and Sun (2018a) developed a novel approach based on the maximum energy dissipation principle to derive the constitutive model for the phase field evolution. This approach will be briefly introduced in the following analysis. In addition, as seen in Eq. (15), the free energy of interfaces, i.e., U, not only depends on the degree of saturation but also on the phase field variable. This reflects the influence of the evolution of pore structure on the free energy of interfaces.

Substituting Eq. (15) into Eq. (14) yields

$$\Phi_{\text{int}} = \boldsymbol{\sigma} : \dot{\boldsymbol{\varepsilon}} + \pi_{eq}\dot{\phi} - \phi\left(p_c + \frac{\partial U}{\partial S_w}\right)\dot{S}_w + \boldsymbol{\xi} \cdot \nabla\dot{d} - \left(\pi + \phi\frac{\partial U}{\partial d}\right)\dot{d} - \dot{\psi}_s \geq 0 \tag{16}$$

where $\pi_{eq} = \overline{p} - U$ is the equivalent pore pressure as originally proposed in Coussy (2004).

Compared with the relatively large compressibility of the porous skeleton as considered in the current study, the solid grain can be assumed incompressible, which leads to $\dot{\phi} = \boldsymbol{\delta} : \dot{\boldsymbol{\varepsilon}}$ (Coussy 2007). Substituting this equality into Eq. (16) gives

$$\Phi_{\text{int}} = \boldsymbol{\sigma}' : \dot{\boldsymbol{\varepsilon}} - \phi\left(p_c + \frac{\partial U}{\partial S_w}\right)\dot{S}_w + \boldsymbol{\xi} \cdot \nabla\dot{d} - \left(\pi + \phi\frac{\partial U}{\partial d}\right)\dot{d} - \dot{\psi}_s \geq 0 \tag{17}$$

$$\boldsymbol{\sigma}' = \boldsymbol{\sigma} + \pi_{\text{eq}}\boldsymbol{\delta} \tag{18}$$

where $\boldsymbol{\sigma}'$ is the effective stress tensor.

Substituting Eq. (15) into Eq. (16) and reformulating the resultant inequality lead to

$$\Phi_{\text{int}} = \left(\boldsymbol{\sigma}' - \frac{\partial \psi_s}{\partial \boldsymbol{\varepsilon}} \right) : \dot{\boldsymbol{\varepsilon}} - \phi \left(p_c + \frac{\partial U}{\partial S_w} \right) \dot{S}_w + \boldsymbol{\xi} \cdot \nabla \dot{d} - \left(\pi + \phi \frac{\partial U}{\partial d} + \frac{\partial \psi_s}{\partial d} \right) \dot{d} \geq 0 \tag{19}$$

By applying the standard Coleman–Noll argument to the inequality above, the constitutive relations for the effective stress tensor, $\boldsymbol{\sigma}$, the capillary pressure, p_c, can be derived as (Na and Sun 2018; Lorenzis et al. 2016)

$$\boldsymbol{\sigma}' = \frac{\partial \psi_s}{\partial \boldsymbol{\varepsilon}}, \tag{20}$$

$$p_c = -\frac{\partial U}{\partial S_w}. \tag{21}$$

In the last term of Eq. (19), the internal microforce can be decomposed into an energetic part, π^{en} and a dissipative part, π^{dis}, which is expressed as (Choo and Sun 2018a, b)

$$\pi = \pi^{\text{en}} + \pi^{\text{dis}} \tag{22}$$

Following the standard Coleman–Noll statement again, the energetic part of the internal microforce can be determined as

$$\pi^{\text{en}} = -\frac{\partial \psi_s}{\partial d} - \phi \frac{\partial U}{\partial d} \tag{23}$$

At this moment, the final form of the Clausius–Duhem inequality can be simplified as

$$\Phi_{\text{int}} = \boldsymbol{\xi} \cdot \nabla \dot{d} - \pi^{\text{dis}} \dot{d} \geq 0 \tag{24}$$

The specific forms for the microforces, i.e., $\boldsymbol{\xi}$ and π^{dis}, will be given in the following section.

3.2.3 Constitutive Models

The gas-driven fracturing in bentonite is mainly caused by the tensile load exerted by the highly pressurized gas. To avoid the compression-induced fracturing, the free energy of the solid matrix is decomposed into a tensile part, $\psi_{s0}^{e+}(\boldsymbol{\varepsilon})$ and a compressive part, $\psi_{s0}^{e-}(\boldsymbol{\varepsilon})$, where only the tensile part serves as the driving force for the fracturing process, which is expressed as

$$\psi_s^e(\boldsymbol{\varepsilon}^e, d) = g(d) \psi_{s0}^{e+}(\boldsymbol{\varepsilon}) + \psi_{s0}^{e-}(\boldsymbol{\varepsilon}) \tag{25}$$

where $g(d)$ is a degradation function.

In this paper, a widely used quadratic degradation function, as expressed by Eq. (26), is adopted to degrade the tensile part of the free energy.

$$g(d) = (1-k)(1-d)^2 + k \tag{26}$$

where k is a small positive value to avoid the singularity of stiffness matrix (Bourdin et al. 2000).

By using the spectral decomposition technique, as done in Miehe et al. (2010a), the tensile part and the compressive part of the free energy of solid matrix can be expressed as

$$\psi_{s0}^{e\pm}(\boldsymbol{\varepsilon}) = \lambda\langle\varepsilon_1 + \varepsilon_2 + \varepsilon_3\rangle_{\pm}^2/2 + \mu\big(\langle\varepsilon_1\rangle_{\pm}^2 + \langle\varepsilon_2\rangle_{\pm}^2 + \langle\varepsilon_3\rangle_{\pm}^2\big) \tag{27}$$

where λ and μ are the Lamé parameters, $\langle x\rangle_{\pm} = (x \pm |x|)/2$ is the Macaulay bracket, and $\{\varepsilon_a\}_{a=1,2,3}$ are the principal components of the strain tensor.

The effective stress tensor can be derived by substituting Eqs. (25)–(27) into Eq. (20) as

$$\boldsymbol{\sigma}'(\boldsymbol{\varepsilon}, d) = g(d)\boldsymbol{\sigma}'^{\pm}(\boldsymbol{\varepsilon}) + \boldsymbol{\sigma}'^{-}(\boldsymbol{\varepsilon}) \tag{28}$$

$$\boldsymbol{\sigma}'^{\pm}(\boldsymbol{\varepsilon}) = \sum_{a=1}^{3}\Big[\lambda\langle\varepsilon_1 + \varepsilon_2 + \varepsilon_3\rangle_{\pm} + 2\mu\langle\varepsilon_a\rangle_{\pm}\Big]\mathbf{n}_a \otimes \mathbf{n}_a \tag{29}$$

where $\boldsymbol{\varepsilon} = \frac{1}{2}\big[\nabla\mathbf{u} + (\nabla\mathbf{u})^T\big]$, $\mathbf{u}$ is the displacement vector, $\boldsymbol{\sigma}'^{\pm}$ are the tensile and compressive parts of the effective stress tensor, and $\{\mathbf{n}_a\}_{a=1,2,3}$ is the principal vector corresponding each principal strain.

Substituting Eqs. (18) and (28) into Eq. (5) gives the specific momentum balance law of the macroforce system as.

$$\nabla \cdot \big[g(d)\boldsymbol{\sigma}'^{\pm}(\boldsymbol{\varepsilon}) + \boldsymbol{\sigma}'^{-}(\boldsymbol{\varepsilon}) - \pi_{\text{eq}}\boldsymbol{\delta}\big] + \rho\mathbf{g} = \mathbf{0}. \tag{30}$$

The specific forms for the internal microforces, i.e., $\boldsymbol{\xi}$ and π^{dis}, can be determined by using the approach proposed by Choo and Sun (2018a). This approach is briefly introduced here for completeness. More details and discussions on it can be found in Choo and Sun (2018a, b). The approach is essentially developed on the postulate that the evolution of the phase field variable can maximize the energy dissipation, i.e., Eq. (24). To this end, the negative of the fracture dissipation functional should be minimized with the following constraint:

$$\left(\frac{d}{l}\right)\dot{d} + l\nabla d\big(\nabla\dot{d}\big) = \dot{\Gamma}_d \tag{31}$$

where l is a characteristic length controlling the width of the phase field and Γ_d is the crack density functional that is used to regularize the sharp discontinuity.

To solve this constrained minimization problem, a Lagrangian can be constructed as

$$L\big(\dot{d}, \nabla\dot{d}, \Lambda\big) = -\boldsymbol{\xi} \cdot \nabla\dot{d} + \pi^{\text{dis}}\dot{d} + \Lambda\left[\left(\frac{d}{l}\right)\dot{d} + l\nabla d\big(\nabla\dot{d}\big) - \dot{\Gamma}_d\right] \tag{32}$$

where Λ is the Lagrangian multiplier.

By applying the stationary condition for the proposed Lagrangian, i.e., Eq. (32), the internal microforce $\boldsymbol{\xi}$ and π^{dis} can be determined as (Choo and Sun 2018a)

$$\boldsymbol{\xi} = \Lambda l\nabla d \tag{33}$$

$$\pi^{\text{dis}} = -\Lambda d/l \tag{34}$$

As analyzed in Choo and Sun (2018a), the Lagrangian multiplier can be interpolated as the critical fracture energy, i.e., $\Lambda = G_c$. Then, substituting Eqs. (33), (34) and (23) into Eq. (9) yields the microforce balance law as

$$G_c l \nabla^2 d - g'(d)\psi_{s0}^{e+} - G_c d/l - \phi \frac{\partial U(S_w, d)}{\partial d} = 0 \tag{35}$$

The interfacial energy in intact porous media, $U(S_w)$, is defined with respect to the capillary pressure, p_c, as (Coussy 2004):

$$U(S_w) = \int_{S_w}^{1} p_c(S)\mathrm{d}S \tag{36}$$

In Eq. (36), the capillary pressure is defined as a function of degree of saturation, which leads to the water retention model. The water retention capability of the developed fractures is inferior to that of porous matrix, since the size of the fractures is much larger than that of porous matrix. Therefore, at a given degree of saturation, the interfacial energy of the fractures is less than that of the porous matrix. In order to account for the fracturing effect, the interfacial energy should also be defined with respect to the phase field variable. In analogy to the degradation of the free energy of solid matrix, i.e., Eq. (25), the interfacial energy can be defined as

$$U(S_w, d) = (1 - d)^{n_U} U(S_w) \tag{37}$$

where n_U is a positive value controlling the degradation of the interfacial energy. With the increase of n_U, the degradation of the interfacial energy will be more sensitive to the change of the phase field variable. The value of n_U may depend on the specific material in which the fracturing takes place. If n_U takes 2, substituting Eq. (37) into Eq. (35) yields a standard governing equation for the phase field, as derived in (Mauthe and Miehe 2017):

$$(1 - d)H^+ - (d - l^2 \nabla^2 d) = 0 \tag{38}$$

$$H^+ = \frac{2(\psi_{s0}^{e+} + \phi U(S_w))}{G_c/l} \tag{39}$$

where H^+ is the fracture driving force functional. It is worth noting that the standard governing equation for phase field, i.e., (38), may not be obtained if the interfacial energy took other forms than the one in (37). More theoretical and experimental works need to be conducted to determine a specific form for the degraded interfacial energy. However, this is out of the scope of the current study.

As seen in Eq. (39), the interfacial energy between wetting and nonwetting fluids has been analytically added to the fracture driving force functional based on the theory of thermodynamics. However, the real contribution of the interfacial energy to the fracturing process in porous media is still under discussion. The experimental and numerical studies in Shin and Santamarina (2011) highlighted the effect of air–water interfaces on the desiccation cracking. Moreover, the grain-scale model in Jain and Juanes (2009) indicated that the capillary effects may influence the gas pressure required for fracturing in saturated porous media. In contrast, Espinoza and Santamarina (2012) stated that capillary-driven fractures may not likely occur in porous media of low porosity that is subjected to high effective stress. This statement may be applied to the current research topic, as the saturated bentonite sample can be considered as a low porosity media (if the adsorbed water is regarded as a part of solid grain) that has a larger swelling pressure at the beginning of gas injection. Importantly, the previous experimental studies on gas migration in saturated

bentonite rarely, if ever, examined the capillary effect on the fracturing process. Instead, these experimental studies mainly concluded that the gas entry mainly occurs when gas pressure reaches the sum of swelling pressure and the porewater pressure (Graham et al. 2012; Harrington et al. 2019; Harrington and Horseman 2003). As analyzed above, the free energy of interfaces will not be examined in the current study but may be considered in the future when enough experimental findings are available.

In addition, previous experimental studies, such as Graham et al. 2012; Harrington et al. 2019 showed that the developed fractures may self-heal after the gas breakthrough phenomenon. This self-healing behavior may involve complex interactions between fluids (water/gas) and clay minerals. For simplicity, the gas-driven fracturing is assumed as an irreversible process in this study, while the self-healing behavior is left for the future study. To achieve this irreversibility, the driving force H^+ in Eq. (38) without considering the free energy of interfaces is replaced by its maximum value during the loading history, H_M^+, as adopted in Miehe et al. (2010a), Choo and Sun (2018a):

$$H_M^+ = \max_{\tau \in [0,t]} \left\{ \frac{2\psi_{s0}^{e+}}{G_c/l} \right\} \tag{40}$$

3.3 Effect of Initial Stress State

Previous experimental studies showed that major gas entry occurs when gas pressure reaches the sum of the swelling pressure and the porewater pressure (Graham et al. 2012; Horseman et al. 1999; Cuss et al. 2014). The swelling pressure can be considered as the effective stress to which the saturated bentonite is initially subjected for a high swelling clay (Horseman et al. 1999). Therefore, the initial stress state is an important factor controlling the fracturing process. Previous phase field models rarely considered the effect of initial stress state, except for the one in Zhou et al. (2020). In that model, the initial stress state is accounted for by incorporating the strain energy caused by the initial stress state (i.e., the product of the initial stress tensor and the strain tensor) into the historical maximum driving force, i.e., Eq. (40). The model was able to capture some desirable features during the hydraulic fracturing process. However, the proposed approach seems not sufficient to identify the effective component of an anisotropic stress state that drives the fracturing process. It is worth noting that the anisotropy concerned in this section is associated with the stress state, rather than the material properties. In this paper, a new approach will be proposed to reasonably describe the effect of the initial stress state on the fracturing process.

Prior to developing a general approach in two dimensions or three dimensions, a one-dimensional tensile test on a bar that is initially in compressive state, as seen in Fig. 2a, is analyzed. Figure 2b shows the stress–strain relationship of this tensile test. With the increase of the tensile strain, the stress within the bar increases from the initial compressive stress, σ_0, to zero, i.e., the stress-free state (corresponding to the dashed configuration in Fig. 2a). At this point, the corresponding tensile strain, ε_{t1}, can be easily determined as

$$\varepsilon_{t1} = -\frac{\sigma_0}{E} \tag{41}$$
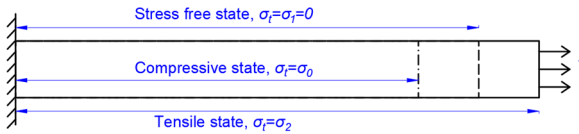
(a) 1-D bar under tensile load

(The dotted dashed line represents the bar under the compressive state, the dashed line corresponds to the stress-free state, and the solid line to the tensile state)
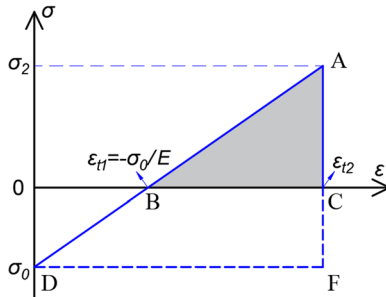
(b) Stress-strain relationship of the 1-D bar (E is the Young's modulus of the bar)

Fig. 2 A 1-D bar under tensile load and its stress–strain relationship

As the tensile strain further increases, the bar begins to be subjected to the tensile stress, see Fig. 2b. Clearly, it is the elastic tensile strain energy under tensile stress state that provides the driving force for the fracturing process. The elastic tensile strain energy, ψ_{ten}, is represented by the area of the grey triangle in Fig. 2b, which can be easily calculated as

$$\psi_{\text{ten}} = \frac{1}{2} E \left(\varepsilon_{t2} - \varepsilon_{t1} \right)^2 \tag{42}$$

Alternatively, the above strain energy can be determined by subtracting the elastic compressive strain energy, ψ_{comp} (represented by the trapezoid BCFD), from the total elastic strain energy, ψ_{tot} (represented by the triangle ADF), which is formulated as

$$\psi_{\text{ten}} = \psi_{\text{tot}} - \psi_{\text{comp}} \tag{43}$$

Here, we can introduce a fictitious initial strain that corresponds to the initial compressive stress as

$$\varepsilon_0 = \frac{\sigma_0}{E} \tag{44}$$

Combining Eqs. (41)–(44), the elastic tensile strain energy can be reformulated as

$$\psi_{ten} = \frac{1}{2} E \left(\varepsilon_{t2} + \varepsilon_0 \right)^2 \tag{45}$$

It can be seen from Eq. (45) that the initial stress state has been accounted for in the elastic tensile strain energy functional by transforming the initial stress into its corresponding strain. Therefore, we can assume that the tensile test on the pre-stressed bar

can be decomposed into two loading steps, i.e., a stress-free bar is loaded to a compressive state (i.e., the bar configuration transforms from the dashed line to the dotted dashed line in Fig. 2a) and then a tensile load is applied on the bar (i.e., the right end of the bar extends from the dotted dashed line to the solid line in Fig. 2a) until fracturing occurs. Clearly, the first step is an imaginary process, while the second one is the real loading process. It is the overall strain, i.e., the sum of strains in the first and in the second step, that determines the elastic tensile strain energy for fracturing process, see Eq. (45).

The 1-D bar analysis given above can be easily extended to either the 2-D or 3-D case. For a general dimensional condition, the fictitious initial strain tensor can be determined as

$$\boldsymbol{\varepsilon}_0 = \mathbb{C} : \boldsymbol{\sigma}_0 \tag{46}$$

where $\mathbb{C}$ is the elastic compliance tensor, $\boldsymbol{\varepsilon}_0$ is the fictitious initial strain tensor corresponding to the initial stress tensor, $\boldsymbol{\sigma}_0$. It is worth noting that $\boldsymbol{\sigma}_0$ here represents the initial stress tensor for pure mechanical problems, while it is interpreted as the initial effective stress tensor for poromechanical problems.

Then, the modified strain tensor, $\tilde{\boldsymbol{\varepsilon}}$, can be determined as

$$\tilde{\boldsymbol{\varepsilon}} = \boldsymbol{\varepsilon}_0 + \boldsymbol{\varepsilon} \tag{47}$$

Therefore, the initial stress state can be naturally accounted for in the phase field model by replacing the strain tensor $\boldsymbol{\varepsilon}$, in Eqs. (25), (27), (28), (29) and (30) by the modified strain tensor, $\tilde{\boldsymbol{\varepsilon}}$. As seen from Eqs. (27) and (29), it is the positive principal strains of the modified strain tensor, $\tilde{\boldsymbol{\varepsilon}}$, that provide the driving force for the fracturing process. Clearly, the different contributions of the three principal components of an anisotropic stress state can be easily identified in this proposed approach.

For a plane strain problem, the specific components of the fictitious strain tensor in Eq. (46) can be expressed as

$$\begin{cases} \varepsilon_{0xx} = \dfrac{1+\nu}{E}\left[(1-\nu)\sigma_{0xx} - \nu\sigma_{0yy}\right] \\[2mm] \varepsilon_{0yy} = \dfrac{1+\nu}{E}\left[(1-\nu)\sigma_{0yy} - \nu\sigma_{0xx}\right] \\[2mm] \varepsilon_{0xy} = \dfrac{1+\nu}{E}\sigma_{0xy} \end{cases} \tag{48}$$

where σ_{0xx}, σ_{0yy}, ε_{0xx}, ε_{0yy} are the normal stress and strain in the x and y directions, respectively, σ_{0xy} and ε_{0xy} are shear stress and strain components, E is the Young's modulus and ν is the Poisson's ratio.

As seen in Eq. (48), for a strong anisotropic stress tensor, the normal strain components may become positive even when both the normal stress components are negative. Then, the tensile elastic strain energy, i.e., ψ_{s0}^{e+} in Eq. (27), becomes positive, and the phase field variable increases according to the fracture-driven force functional, i.e., Eq. (40). Note that the contribution of the interfacial energy is not considered here. This means that the fracture can develop even though the material is subject to fully compressive stress. Clearly, this result is not consistent with the reality. To avoid this issue caused by the Poisson's effect, a stress-based fracture driving force functional, originally proposed in Miehe et al. (2015), can be used to govern the fracturing process. This driving force functional is expressed as

$$H_M^+ = \max_{\tau \in [0,t]} \left\{ \zeta \left\langle \sum_{a=1}^{3} \left(\frac{\langle \sigma_a' \rangle_+}{\sigma_{cr}} \right)^2 - 1 \right\rangle_+ \right\}$$

(49)

where $\{\sigma_a'\}_{a=1,2,3}$ is the principal effective stress, σ_{cr} is a critical tensile stress and ζ is a dimensionless parameter that controls the evolution of phase field after the critical tensile stress is reached. As seen in Eq. (49), the driving force functional is proportional to the ζ after the critical stress is exceeded. Thus, with the increase of ζ, the fracturing process will be accelerated. As presented in Miehe et al. (2015), a larger value of ζ can lead to a more rapid increase of the phase field variable.

Hereafter, the energy-based fracture driving force functional, i.e., Eq. (40), is termed as a Griffith fracture criterion (GFC), while the stress-based functional, i.e., Eq. (49), is called a Rankine-type fracture criterion (RFC). Both fracture criteria will be examined in terms of their performances in controlling the fracturing process in Sect. 6.

4 Hydraulic Model

4.1 Mass Balance Equations

The mass balance equations for gas and water in porous media can be derived based on the Biot's consolidation theory (Taron et al. 2009; Taron and Elsworth 2009), mixture theory (Choo and Sun 2018b; Borja and Koliji 2009; Choo et al. 2016) or the theory of porous media (Heider and Sun 2020). The final forms of these equations are similar to each other. Here, based on the assumption of small deformation and incompressible solid grain, the mass balance equations for gas and water can be expressed as

$$\rho_g \phi \left(\frac{S_g}{K_g} - \frac{\partial S_e}{\partial p_c} \right) \frac{\partial p_g}{\partial t} + \nabla \cdot (\rho_g \mathbf{v}_g^D) = -\rho_g \phi \frac{\partial S_e}{\partial p_c} \frac{\partial p_w}{\partial t} - S_g \rho_g \frac{\partial \varepsilon_v}{\partial t}$$

(50)

$$\rho_w \phi \left(\frac{S_w}{K_w} - \frac{\partial S_e}{\partial p_c} \right) \frac{\partial p_w}{\partial t} + \nabla \cdot (\rho_w \mathbf{v}_w^D) = -\rho_w \phi \frac{\partial S_e}{\partial p_c} \frac{\partial p_g}{\partial t} - S_w \rho_w \frac{\partial \varepsilon_v}{\partial t}$$

(51)

where K_κ is the bulk modulus of fluid κ (κ denotes w and g for water and gas, respectively), S_e is the effective degree of saturation, ε_v is the volumetric strain and $\mathbf{v}_\kappa^D$ is the Darcy's velocity.

4.2 Constitutive Models

The dissipation due to the viscous fluid flow in porous space is expressed as

$$\varphi_f = \left(-\nabla p_w + \rho_w \mathbf{g} \right) \cdot \mathbf{v}_w^D + \left(-\nabla p_g + \rho_g \mathbf{g} \right) \cdot \mathbf{v}_g^D \geq 0$$

(52)

To ensure the positiveness of the dissipation due to the viscous fluid flow, the fluid flux can be described by a generalized Darcy's law,

$$\mathbf{v}_\kappa^D = -\frac{\mathbf{k}_{in} k_{r\kappa}}{\mu_\kappa} (\nabla p_\kappa - \rho_\kappa \mathbf{g}) \tag{53}$$

where $\mathbf{k}_{in}$ is the intrinsic permeability tensor, $k_{r\kappa}$ is the relative permeability and μ_κ is the fluid dynamic viscosity.

When fluid flows through expansive clays, there might be interactions between the fluid and clay minerals. To account for this interaction, the traditional Darcy's law has been modified in Bennethum et al. (1997), Achanta et al. (1994). However, for simplicity, this interaction will not be considered in the current study. Therefore, the generalized Darcy's law, i.e., Eq. (53), will be used to simulate the two-phase flow in expansive soils, as done in Olivella and Alonso (2008), Sánchez et al. (2016), Gens Solé et al. (2011).

In the following part of this section, two sets of hydraulic properties, including the intrinsic permeability, relative permeability and gas entry value, are proposed for the developed fractures and the porous matrix, respectively. As done in Guo and Fall (2019), these two sets of hydraulic properties are connected by a transitional function to describe the corresponding properties in the transition zone between fractures and porous matrix, which can be formulated as

$$P_t = Z(d)P_f + [1 - Z(d)]P_p \tag{54}$$

$$Z(d) = \frac{1}{2}\left\{\tan h\left[\theta_t\left(d - d_{cr}\right)\right] - \tan h\left(-d_{cr}\theta_t\right)\right\} \tag{55}$$

where P_t, P_f and P_p denote the hydraulic properties in the transitional zone, the fractures and the porous matrix, respectively, $Z(d)$ is the transitional function, d_{cr} is a critical value of phase field and θ_t is a parameter controlling the slope of the curve. The numerical result will be sensitive to the parameters adopted in the transitional function. This is because the hydraulic properties around the fracture are significantly influenced by the transitional function. This will then influence the evolution of gas pressure in the fracture and the fracturing process. In this paper, θ_t and d_{cr} are equal to 50 and 0.9, respectively, to achieve the localized feature of gas flow.

4.2.1 Intrinsic Permeability

In the undamaged clay matrix, the intrinsic permeability is assumed to be isotropic. Its evolution with the change of porosity is described by the Kozeny–Carman model (Chapuis and Aubertin 2003):

$$\mathbf{k}_p = k_{p0}\left(\frac{\left(1 - \phi_0\right)^2}{\phi_0^3}\right)\frac{\phi^3}{(1 - \phi)^2}\boldsymbol{\delta} \tag{56}$$

where k_p and ϕ denote the current intrinsic permeability and porosity, respectively, k_{p0} and ϕ_0 represent the corresponding initial values.

In this study, the developed fracture is idealized as an opening between two parallel plates. Then, the anisotropic permeability tensor can be expressed as (Snow 1969)

$$\mathbf{k}_f = \frac{w^2}{12}\left(\mathbf{I} - \mathbf{n}_f \otimes \mathbf{n}_f\right) \tag{57}$$

where $\mathbf{n}_f = \nabla d / |\nabla d|$ is the unit normal vector of the developed fracture, $w = h_e \left(\mathbf{n}_f \cdot \boldsymbol{\varepsilon} \cdot \mathbf{n}_f \right)$ is the fracture aperture (Miehe and Mauthe 2016) and h_e is the element size.

4.2.2 Water Retention Curve

In this paper, the water retention behavior for the unsaturated porous media is described by the van Genuchten model (1980):

$$S_{\vartheta e} = \left[1 + \left(\frac{p_c}{p_{\vartheta \mathrm{gev}}} \right)^n \right]^{-m} \tag{58}$$

where $p_{\vartheta \mathrm{gev}}$ is the gas entry value (ϑ represents f and p for fractures and porous matrix, respectively, $n = 1/(1 - m)$ is a shape parameter.

4.2.3 Relative Permeability

During the imbibition process, some part of gas may be trapped in the porous network and then become immobile (Juanes et al. 2006; Spiteri and Juanes 2006). This may induce a hysteresis phenomenon in the relative permeability. Currently, many models are available to describe this phenomenon, such as those in Doughty (2007), Parker and Lenhard (1987), Lenhard and Parker (1987), Killough (1976). This hysteresis has been considered in Guo and Fall (2018) for describing the effect of gas entrapment on the gas flow behavior in bentonite. However, this hysteresis will not be considered here, since this study focuses on the fracturing process.

In the intact porous matrix, the relative permeabilities for gas and water (k_{prw} and k_{prg}, respectively) are generally described by the Mualem–van Genuchten model (Genuchten 1980; Luckner et al. 1989; Mualem 1976), which are expressed as

$$k_{prw} = \sqrt{S_e} \left[1 - \left(1 - S_e^{1/m} \right)^m \right]^2 \tag{59}$$

$$k_{prg} = \sqrt{1 - S_e} \left(1 - S_e^{1/m} \right)^{2m} \tag{60}$$

Alternatively, the relative permeability of gas is commonly described by a power law, as seen in Olivella and Alonso (2008), Arnedo et al. (2013), Gerard et al. (2014), which is expressed as

$$k_{prg} = \left(1 - S_e \right)^{n_r} \tag{61}$$

where n_r is a model parameter which is taken as 3 in this study.

Figure 3 presents the curves for the Mualem–van Genuchten model, i.e., Eq. (60) with m taken as 0.45, and the power law, i.e., Eq. (61). The two models perform rather differently to describe the relative permeability of gas evolving with the effective degree of saturation. In general, the power law with order of 3 predicts a lower relative permeability of gas than that predicted by the Mualem–van Genuchten model. In particular, the relative permeability of gas given by the power law is close to 0 when the effective degree of saturation ranges between 0.8 and 1. In contrast, the relative permeability of gas given by the Mualem–van Genuchten model has reached approximately 0.2 when the effective degree of saturation is 0.8. Therefore, the power law with order of 3 is more suitable to simulate the low permeable feature of the

Fig. 3 Curves of relative permeability of gas
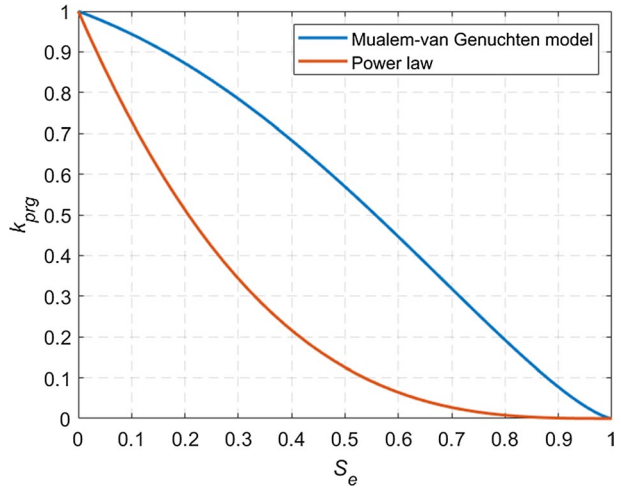
porous matrix adjacent to the developed fracture. In the following sections, the power law model will be used to describe the relative permeability of gas, unless otherwise stated. It is worth noting that a tiny value, i.e., 1×10^{-4}, is added to the power law model, i.e., Eq. (61), to ensure a small gas permeability at the beginning of simulation.

A relative permeability model for fracture was proposed by Fourar and Lenormand (1998). The fracture is idealized as an opening between two parallel planes. The wetting fluid covers the fracture planes, and the non-wetting fluid flows between the two layers formed by the wetting fluid. By assuming Stokes flow in each fluid, the relative permeabilities for water and gas (k_{frw} and k_{frg}, respectively) can be derived as (Fourar and Lenormand 1998; Cueto-Felgueroso and Juanes 2014)

$$k_{frw} = \frac{1}{2} S_w^2 \left(3 - S_w \right) \tag{62}$$

$$k_{frg} = S_g^3 + \frac{3\mu_g}{2\mu_w} S_g \left(1 - S_g^2 \right) \tag{63}$$

5 Model Implementation

5.1 Weak Form and Implementation

The strong forms for the coupled HM-PF model are given as Eqs. (30), (38), (50) and (51). Integrating the product of the strong forms and their corresponding weighting functions results in the weak forms for displacement, water pressure, gas pressure and phase field, which are, respectively, expressed as

$$\boldsymbol{G} = \int_{\Omega} \nabla^{\mathrm{s}} \boldsymbol{\eta} : \boldsymbol{\sigma}' \mathrm{d}\Omega - \int_{\Omega} \bar{p} \nabla \cdot \boldsymbol{\eta} \mathrm{d}\Omega - \int_{\Omega} \boldsymbol{\eta} \cdot \rho \mathbf{g} \mathrm{d}\Omega - \int_{\partial\Omega} \boldsymbol{\eta} \cdot \bar{\mathbf{t}} d\partial\Omega = 0 \tag{64}$$

$$F_w = \int_\Omega \theta_w \left[S_w \nabla \cdot \dot{\mathbf{u}} + \phi \left(\frac{S_w}{K_w} - \frac{\partial S_e}{\partial p_c} \right) \dot{p}_w + \phi \frac{\partial S_e}{\partial p_c} \dot{p}_g \right] d\Omega$$
$$- \int_\Omega \nabla \theta_w \cdot \mathbf{v}_w^D d\Omega - \int_{\partial\Omega} \theta_w \overline{q}_w d\partial\Omega = 0 \tag{65}$$

$$F_g = \int_\Omega \theta_g \left[S_g \nabla \cdot \dot{\mathbf{u}} + \phi \left(\frac{S_g}{K_g} - \frac{\partial S_e}{\partial p_c} \right) \dot{p}_g + \phi \frac{\partial S_e}{\partial p_c} \dot{p}_w \right] d\Omega$$
$$- \int_\Omega \nabla \theta_g \cdot \mathbf{v}_g^D d\Omega - \int_{\partial\Omega} \theta_g \overline{q}_g d\partial\Omega = 0 \tag{66}$$

$$P = \int_\Omega \varphi H_M^+ (1 - d) d\Omega - \int_\Omega \left[\varphi d + l^2 (\nabla \varphi \cdot \nabla d) \right] d\Omega = 0 \tag{67}$$

where $\boldsymbol{\eta}$, θ_w, θ_g and φ are the weighting functions for displacement field, water pressure field, gas pressure field and phase field, respectively.

The weak forms given above are implemented in COMSOL MULTIPHYSICS in which the spatial and temporal discretization can be automatically conducted. In this study, a staggered solution scheme is used to solve the coupled HM-PF model, as also used in Zhou et al. (2018), Mauthe and Miehe (2017), Miehe et al. (2010b), as this staggered approach is more computationally efficient and stable than its monolithic counterpart. The basic steps for this staggered approach are illustrated in Fig. 4.

As seen in Fig. 4, in each time step, the gas pressure, water pressure and displacement vector are first solved based on the phase field that was calculated at the previous iterative step. Secondly, the maximum historical value, H_M^+, is recorded. Then, the phase field is determined by the recorded maximum historical value. If the convergence criterion is fulfilled at this point, the solutions for this time step are updated by using the converged values, and then, the algorithm turns to the next time step until the maximum time step is reached. Otherwise, the previous steps should be iterated until the convergence criterion is fulfilled.

5.2 Stabilized Finite Element

The phase field method for simulating the fracturing propagation requires very fine meshes to clearly track the fracture trajectory. Therefore, the proposed phase field model will be more computationally expensive when coupled with the HM model. It is acknowledged that the adaptive meshing technique and parallel computing method have been developed in Lee et al. (2016) and Wheeler et al. (2020) to enhance the computational efficiency of the phase field method to simulate the fluid-driven fracturing in porous media. These methods for increasing the computational efficiency are out of the scope of this paper. To alleviate the computational effort, the Q4P4 element (where "Q" denotes the number of nodes for displacement tensor and "P" denotes the number of nodes for pore fluid pressure) can be used to discretize the whole simulated domain. As seen in Fig. 5, the Q4P4 element has fewer degrees of freedom and fewer Gauss quadrature points compared with the Q9P4 element. Thus, for a domain discretized by fine meshes, the Q4P4 element is superior to the Q9P4 element in saving computational time. However, the Q4P4 element (where both the pore pressure field and the displacement field are interpolated by a linear shape function) violates the Ladyzhenskaya–Babuška–Brezzi condition, which may lead to the pore
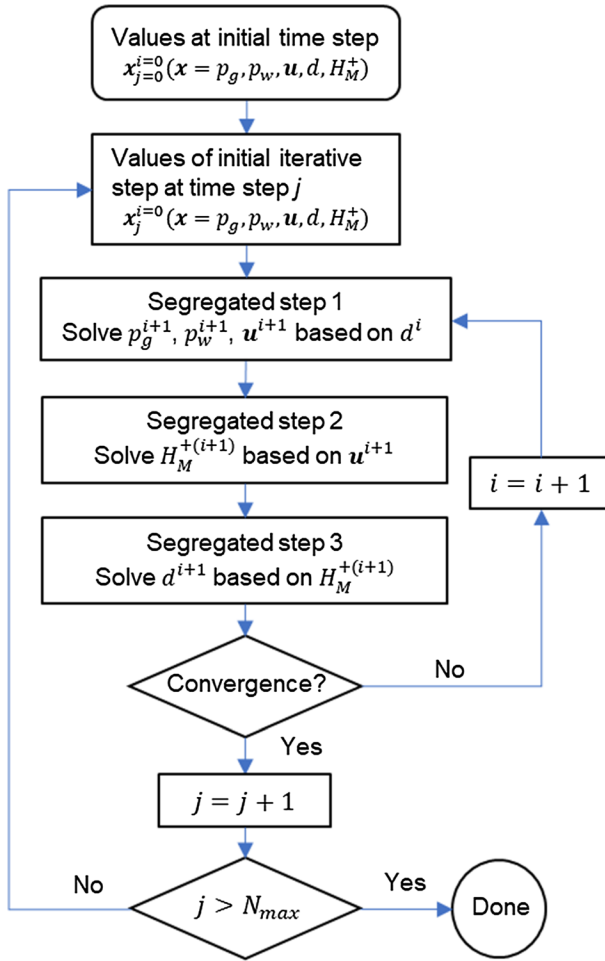
Fig. 4 Staggered solution scheme for the coupled HM-PF model

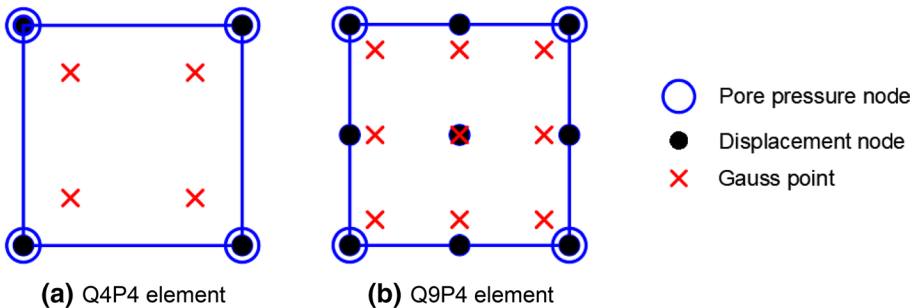**(a)** Q4P4 element   **(b)** Q9P4 element

Fig. 5 Comparison between Q4P4 element and Q9P4 element

pressure oscillation (White and Borja 2008). To avoid this issue, a stabilized method based on the polynomial-pressure-projection technique is generally adopted in the previous literature (White and Borja 2008; Li and Wei 2018; Choo and Borja 2015). This approach is generalized to stabilize both the water pressure and the gas pressure in this study, as also done in Song et al. (2017). In specific, the weak forms for the mass balance equation of gas and water, i.e., Eqs. (65) and (66), are stabilized by adding a stabilized term, F_κ^{stab}, which is expressed as (White and Borja 2008)

$$F_\kappa^{\text{stab}} = \int_\Omega \frac{1}{2G}\left(\theta_\kappa - \prod \theta_\kappa\right)\left(\dot{p}_\kappa - \prod \dot{p}_\kappa\right) \tag{68}$$

where $\prod p_\kappa|_{\Omega^e} = \frac{1}{V^e}\int_{\Omega^e} p_\kappa d\Omega$, V^e denotes the volume of an element, Ω^e is the domain occupied by the element, and G is the shear modulus.

## 6 Model Validation and Simulations

The effect of initial stress state on the fracture initiation and propagation is validated in Sect. 6.1. The gas-driven fracturing in saturated bentonite is simulated in Sect. 6.2 where the effects of initial stress state and boundary conditions on the fracturing process have been examined. It is worth noting that the sign of compressive stress is taken as positive in the section to facilitate the comparison of magnitude.

6.1 Model Validation

Some basic validations for the proposed coupled HM-PF model have been conducted in Guo and Fall (2019), including the pure shear test, the one-dimensional consolidation test and the hydraulic fracturing test. In this section, the main goal of the simulations is to validate that the effect of initial stress state can be well described by the proposed modified strain tensor. Both the isotropic and the anisotropic initial stress states will be examined. For simplicity, only water-driven fracturing will be considered in the following simulations.

Figure 6 shows the simulated domain and boundary conditions. The dimension of the domain is 25 mm in width and 50 mm in height. The center part of the domain is discretized by fine square elements with a size of 0.25 mm, while the other part is discretized by coarser quadrilateral elements to alleviate computational effort. The initial porewater pressure is 1 MPa. The water pressure on the boundary is equal to the initial porewater pressure. The initial stress state will be given in the following subsections. The tractions in the vertical and horizontal directions, i.e., t_v and t_h, are set as values that can achieve an initial stress equilibrium at the boundary. The left boundary is an axis of symmetry, and the point at the left corner is fixed to ensure convergency. The Young's modulus is 307 MPa and the Poisson's ratio is 0.4 (Tamayo-Mas et al. 2018). Here both the RFC and the GFC will be examined in terms of their performance in controlling the fracturing process. The tensile strength is set as 0.5 MPa for the RFC, while the fracture energy is set as 1.0 J/m^2 for the GFC. The initial porosity is 0.044, by assuming that the adsorbed water that accounts for 90% of the total water content is a part of the solid particle (Zheng et al. 2017). The initial permeability of the porous media is assumed to be 3.4×10^{-21} m^2. As adopted in Miehe et al. (2010a), Guo and Fall (2019), the internal length scale, l, is set as twice the element size for all simulations in this paper. An additional mass source, i.e., 0.3 kg/m^3, is applied

Fig. 6 Simulated domain and applied boundary conditions (*Note*: A is a monitoring point that will be used in Sect. 6.2.3)

$\bar{t} = t_v$

A

$\bar{p}_w = p_0$

Axis of Symmetry

Q_g

$\bar{t} = t_h$

$\bar{p}_w = p_0$

$\bar{t} = t_v$
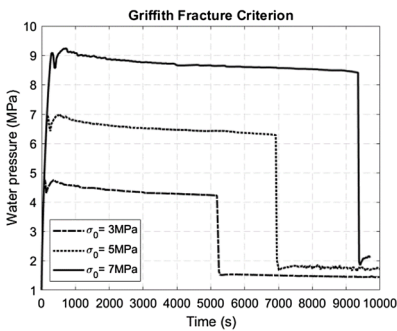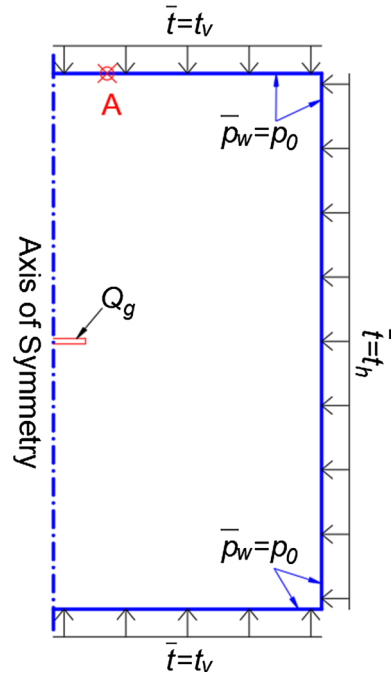
(a) Water pressure at injection zone
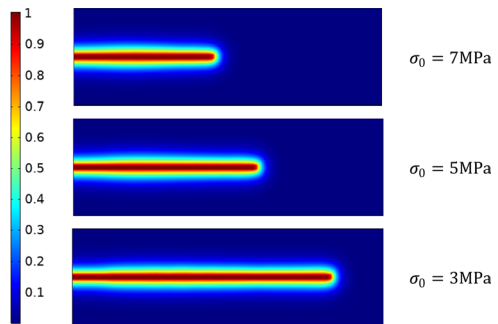
(b) Profiles of phase field at v =5000s

Fig. 7 Simulated water pressure and phase field based on GFC (Note that only the center part of the domain is presented in **b**)

to the red injection zone, as seen in Fig. 6, to simulate the water injection operation. The size of the red zone is 0.25 mm×3 mm in height and width, respectively.

6.1.1 Isotropic Initial Stress State

In this section, the simulated domain is subjected to an isotropic initial stress that is selected as 3 MPa, 5 MPa and 7 MPa in each respective case. Both the GFC and the RFC will be examined in terms of their performances of controlling the fracturing process.

Figure 7a presents the simulated water pressure at the injection zone based on the GFC. For each specific initial stress, the water pressure mainly experiences two peaks. As the water is injected into the injection zone, the water pressure increases rapidly until reaching the first peak at which the GFC is fulfilled, as seen in Fig. 7a. Then, a tensile failure occurs in the injection zone. This leads to a rapid volume dilation, and as a result, a drop of water pressure in the injection zone. In contrast, the second peak is associated with the fracture propagation toward the right boundary. The extension of the fracture has increased the volume of the fracture space at a higher rate than the water injection rate, thus leading to the continuous drop of water pressure after the second peak, as seen in Fig. 7a.

For each case of initial stress, the water pressure at the first peak has exceeded the total stress (the sum of the initial porewater pressure and the initial stress) by a certain small value that corresponds to the fracture energy required by the GFC. In addition, corresponding to each increasing step, i.e., 2 MPa, in the initial stress, the water pressure required to trigger the fracturing process increases in a comparable step. As seen in Fig. 7a, the curves after the second peak are almost parallel to each other with a difference of approximately 2 MPa. When the fracture reaches the right boundary, the water flows out of the domain rapidly, thus leading to an abrupt decrease of water pressure. As seen in Fig. 7a, the fracture that is developed under lower initial stress firstly reaches the right boundary, since less water content is required to induce the fracture propagation. This is also observed in Fig. 7b where the phase field profiles with lower initial stress at $t = 5000$ s are closer to the right boundary.

Figure 8a presents the simulated water pressure at the injection zone based on the RFC. In general, the evolution curves of water pressure are very similar to those determined by using the GFC. With the increase of the initial stress, the water pressure at peak increases by an approximately equal value. The peak value of the water pressure is just above a critical value, i.e., the sum of the total stress and the tensile strength (i.e., 0.5 MPa). As the fracture propagates toward the right boundary, the water pressure at the injection zone is maintained around the critical value. In addition, the fracture propagates faster under lower initial stress than under higher initial pressure, see Fig. 8a, b. This is consistent with the numerical results based on the GFC.

As analyzed above, the effect of initial stress state can be well described by adopting the modified stain tensor, i.e., Eq. (47), in the phase field model. Both the GFC and the RFC can realistically simulate the fracture propagation under isotropic initial stress state. Here,
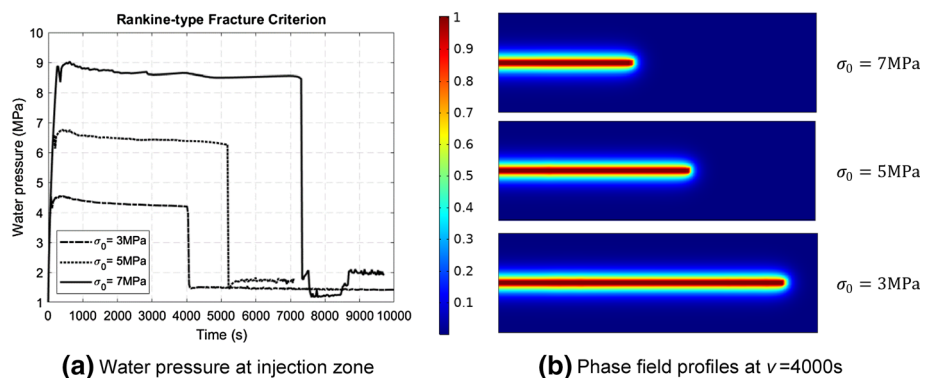

(a) Water pressure at injection zone   **(b)** Phase field profiles at $v = 4000$s

Fig. 8 Simulated water pressure and phase field profiles based on RFC

it is worth noting that the coupled HM-PF models based on the GFC are more computationally efficient than those based on the RFC which needs an additional spectral decomposition on the stress tensor, see Eq. (49).

6.1.2 Anisotropic Initial Stress State

As discussed in Sect. 3.3, the phase field model based on GFC is not appropriate to simulate the fracture propagation in anisotropic initial stress field because of the Poisson's effect. In this section, therefore, only the RFC will be examined in terms of its performance of simulating the fracturing process under anisotropic initial stress state. Five groups of vertical and horizontal initial stresses, i.e., (3 MPa, 5 MPa), (4 MPa, 5 MPa), (5 MPa, 6 MPa), (5 MPa, 7 MPa) and (7 MPa, 5 MPa), are used to conduct the sensitivity analysis. Figure 9 presents the profiles of phase field under different anisotropic initial stress states. For the first four groups of stress combination as given above (where the horizontal stress is larger than the vertical one), the fractures propagate along the horizontal direction, see Fig. 9a–d. In contrast, for the last group of stress combination (where the horizontal stress is less than the vertical one), the fracture propagates vertically, although the initial injection zone is predefined horizontally, see Fig. 9e. This numerical result is consistent with the fracturing theory that the fracture propagates along the direction that is perpendicular to the minimum principal stress.

Figure 10 shows the evolutions of water pressure at the injection zone under different anisotropic initial stress states. For the first four groups of stress combination, the water pressure required to trigger the fracture propagation is approximately equal to the sum of the initial vertical stress, the porewater pressure and the tensile strength. When the vertical stress is fixed at 5 MPa, the variation in the horizontal stress has little influence on the evolution of water pressure, as indicated by comparing the dotted green line and the
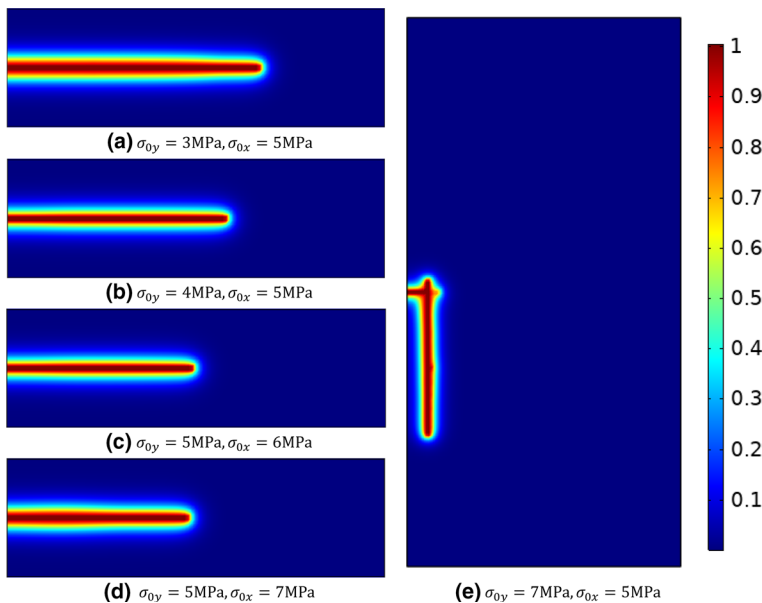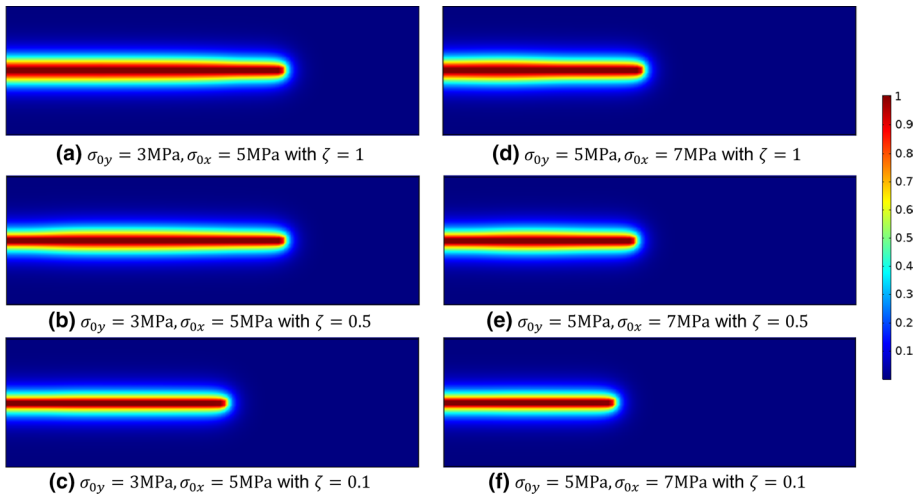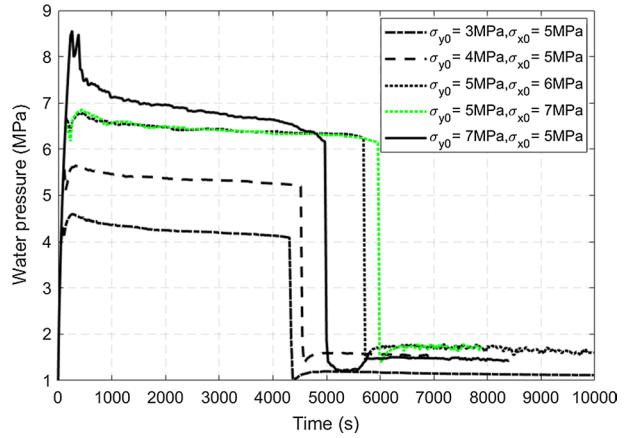

(a) $\sigma_{0y} = 3\text{MPa}, \sigma_{0x} = 5\text{MPa}$

(b) $\sigma_{0y} = 4\text{MPa}, \sigma_{0x} = 5\text{MPa}$

(c) $\sigma_{0y} = 5\text{MPa}, \sigma_{0x} = 6\text{MPa}$

(d) $\sigma_{0y} = 5\text{MPa}, \sigma_{0x} = 7\text{MPa}$

(e) $\sigma_{0y} = 7\text{MPa}, \sigma_{0x} = 5\text{MPa}$

Fig. 9 Profiles of phase field under anisotropic initial stress state at $t = 4000$ s

Fig. 10 Evolutions of water pressure at injection zone with different initial stress states

(a) $\sigma_{0y} = 3\text{MPa}, \sigma_{0x} = 5\text{MPa}$ with $\zeta = 1$

(d) $\sigma_{0y} = 5\text{MPa}, \sigma_{0x} = 7\text{MPa}$ with $\zeta = 1$

(b) $\sigma_{0y} = 3\text{MPa}, \sigma_{0x} = 5\text{MPa}$ with $\zeta = 0.5$

(e) $\sigma_{0y} = 5\text{MPa}, \sigma_{0x} = 7\text{MPa}$ with $\zeta = 0.5$

(c) $\sigma_{0y} = 3\text{MPa}, \sigma_{0x} = 5\text{MPa}$ with $\zeta = 0.1$

(f) $\sigma_{0y} = 5\text{MPa}, \sigma_{0x} = 7\text{MPa}$ with $\zeta = 0.1$

Fig. 11 Profiles of phase field with different values of ζ at $t = 4000$ s

dotted black in Fig. 10. For the last group of stress combination, i.e., ($\sigma_{y0} = 7$ MPa and $\sigma_{x0} = 5$ MPa), the water pressure reaches as high as 8.5 MPa and then declines rapidly, leading to a more distinct peaking stage compared with other cases. The occurrence of the peak value is associated with the predefined horizontal direction of the red injection zone, as seen in Fig. 6. As the horizontal stress is less than the vertical one, the propagation direction switches from the horizontal to the vertical, which leads to the rapid drop of the water pressure, as shown in Fig. 10.

In general, the numerical results as analyzed above prove that the RFC can satisfactorily describe the fracture propagation under an anisotropic initial stress state.

Here, it is worth noting that for the stress combinations in which there is a larger difference between the horizontal stress and the vertical stress, such as (3 MPa, 5 MPa) and (5 MPa, 7 MPa), the width of the phase field profile is relatively larger, see Fig. 9a, d. This means that the developed fracture tends to expand toward the direction of lower principal

stress. As the difference between the horizontal and the vertical stresses increases, the profiles of phase field become more sensitive in the direction of the lower stress component. Through controlling the coefficient, ζ, in Eq. (49), the sensitivity may be alleviated. Figure 11 shows the profiles of phase field for the initial stress combinations, i.e., (3 MPa, 5 MPa) and (5 MPa, 7 MPa), with the coefficient ζ decreased from 1 to 0.1. Clearly, with the decrease of the coefficient, ζ, both the width of the phase field profile and the rate of fracture propagation have decreased.

6.2 Gas-Driven Fracturing in Saturated Bentonite

The simulated domain in Sect. 6.1 is adopted in the following simulations. The initial gas pressure and the initial water pressure for the entire domain are set as 1.05 MPa and 1.0 MPa, respectively. The slight variation between the initial gas pressure and the initial water pressure is to avoid the convergence issue. The gas entry value for the injection zone is set as an extremely small value, i.e., 10 Pa, to ensure the injection zone is saturated with gas phase. The gas entry value for the remaining domain is set as 18 MPa (Tamayo-Mas et al. 2018). Therefore, the gas pressure in the injection zone fully contributes to the pore pressure, which makes tensile failure possible in the injection zone. Conversely, if the gas entry value of the injection zone is equal to 18 MPa, the gas can hardly enter the pore and therefore contributes little to the rise of pore pressure. The gas entry value for the developed fractures is set as 5 Pa. The shape parameter, m, in the van Genuchten model is 0.45 (Tamayo-Mas et al. 2018). For simplicity, the intrinsic permeability for the developed fracture is assumed to be ten times of the permeability for porous matrix. The other hydromechanical properties are the same as those in Sect. 6.1. The mass injection rate applied on the injection zone is 0.001 kg/(m^3 s). The top and bottom boundaries are impermeable to water and gas. A mass flux is applied on the right boundary for both the gas pressure and water pressure field, as expressed by Eq. (69) (Guo and Fall 2018). The other boundary conditions are the same as those in Sect. 6.1.1, unless otherwise stated.

$$q_{\kappa o} = \begin{cases} \rho_\kappa \frac{k_{in}k_{r\kappa}}{\mu_\kappa l_q}\left(p_\kappa - p_{\kappa cr}\right), & p_\kappa > p_{\kappa cr} \\ 0, & p_\kappa \leq p_{\kappa cr} \end{cases} \tag{69}$$

where $p_{\kappa cr}$ is a critical pressure over which the fluid outflow is allowed, and l_q is a characteristic length. In the following simulations, the critical pressure is just higher than the initial fluid pressure and the critical length is set as 1 mm.

As the swelling pressure for expansive soils is generally considered as an isotropic value, both the GFC and the RFC can be used to describe the fracturing process. In this section, the GFC is used, as it is more computationally efficient. According to the experimental result in Wang et al. (2007), the fracture toughness of the used clay is between 7.10 and 31.43 kPa m$^{0.5}$. Then, the fracture energy of the clay can be determined as

$$G_c = \frac{K_{IC}^2}{E'} \tag{70}$$

where K_{IC} is the fracture toughness and E' is the Young's modulus under the plane strain condition.

Then, the fracture energy ranges between 0.14 and 2.70 J/m^2. For simplicity, the fracture energy for the current bentonite material is assumed to be 1 J/m^2, as it has not yet been

reported in previous studies. To realistically simulate the fracturing process in bentonite, more experimental studies on the fracturing energy need to be conducted in the future.

6.2.1 Effect of Initial Stress State

In this section, the simulated domain is subjected to a constant confining pressure on the outside boundaries. Three different isotropic initial stress states, i.e., 4.8 MPa, 5.8 MPa and 6.8 MPa, are examined in terms of their effects on the fracturing behavior. Figure 12a presents the evolutions of gas pressure at the injection zone under the three initial stress states. For each case of the initial stress, the gas pressure mainly experiences two peaks and a series of fluctuations. As mentioned in Sect. 6.1.1, the first peak is associated with the

Fig. 12 Evolutions of gas pressure and profiles of phase field under different initial stress states

(a) Evolutions of gas pressure at the injection zone

(1) $\sigma_0 = 6.8$MPa

(2) $\sigma_0 = 5.8$MPa

(3) $\sigma_0 = 4.8$MPa
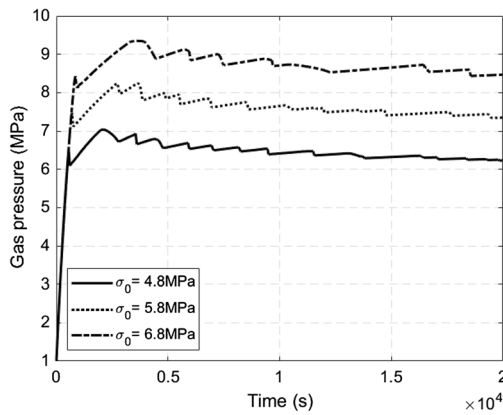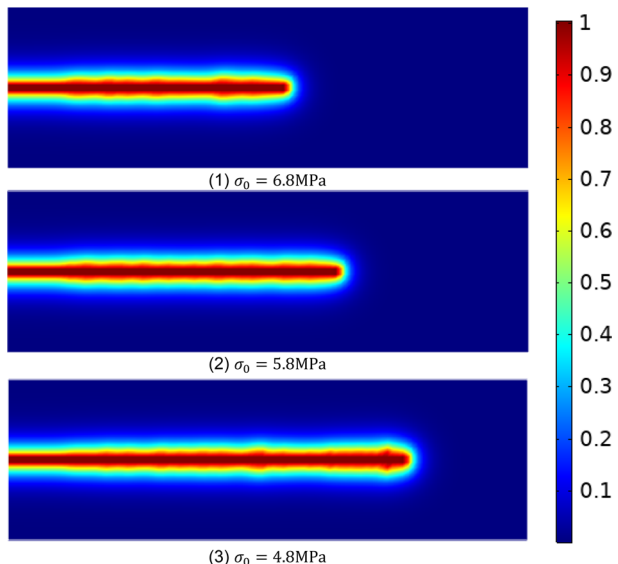
(b) Profiles of phase field at time t=20000s

failure of the injection zone, while the second one represents the value required to trigger the fracture propagation. The second peak value in general exceeds the sum of the initial stress and the initial porewater pressure by a certain value that corresponds to the fracture energy. As a larger amount of gas is required to trigger the fracturing process under higher initial stress, the length of the developed fracture at a specific moment is smaller than its counterpart under lower initial stress, see Fig. 12b. In addition, corresponding to the increase step, i.e., 1 MPa, in the initial stress state, the first and the second peak values also have a similar increase step with their respective values in the adjacent evolution curve. In general, the three evolution curves are almost parallel to each other with a similar increase step during the whole period of gas injection. Therefore, this numerical result validates that the effect of the swelling pressure (regarded as the initial stress in this paper) has been appropriately accounted for by using the modified strain tensor and the GFC.

6.2.2 Effect of Boundary Condition

In this section, the effect of boundary condition on the hydromechanical behaviors, including gas pressure, water pressure, total stress and boundary displacement, is examined. To simulate different boundary stiffnesses, a spring-type boundary condition is added to the outside boundaries. As the domain expands outwards under high gas pressure, the spring-type boundary provides an additional compressive load to restrain the expansion tendency. The normal stiffness, k_n, of the spring varies from 0 GPa/m, 60 GPa/m, 120 GPa/m, 240 GPa/m, 480 GPa/m to $+\infty$ GPa/m. Clearly, the normal stiffnesses, 0 GPa/m and $+\infty$ GPa/m, represent the CCC and the CVC, respectively. The shear stiffness of the boundary is assumed to be zero in the current study. Here it is noted that the constant pressure on the outside boundaries is maintained to achieve the initial stress equilibrium. The initial stress of the domain is set as 5.8 MPa.

Figure 13a presents the evolutions of water pressure at a monitoring point A, as marked in Fig. 6. A higher boundary stiffness leads to a higher water pressure at the monitoring point, since the water under a more rigid boundary condition is compressed more significantly by the highly pressurized gas. This can be observed in Fig. 13b where the vertical displacement at the monitoring point decreases with the increase of boundary stiffness. Under the CVC, the dilation is totally prohibited on the boundary, see the red line in Fig. 13b, which leads to a high sensitivity of water pressure to the deformation within the simulated domain. As shown by the red line in Fig. 13a, the water pressure presents a rapid increase at the very beginning of gas injection. Similar to the evolution of water pressure, the total stress can reach a higher value under the boundary condition with larger stiffness, seen in Fig. 13c. At the monitoring point A, the degree of saturation remains almost one during the period of gas injection (as will be discussed in the next subsection), and therefore, the porewater pressure fully contributes to the total stress. Then, the Terzaghi's effective stress is recovered. By comparing Fig. 13a, c, it can be found that the change of total stress mainly results from the change of water pressure, while the contribution of effective stress is less for any level of boundary stiffness. This means that the deformation at the monitoring point is less even under boundary condition with lower stiffness. The dilation of the boundary under CCC mainly results from the opening of the developed fracture.

Figure 14a shows the evolutions of gas pressure at the injection zone with different boundary stiffnesses. The gas pressure required to maintain the fracturing process is higher for the case of larger boundary stiffness. In specific, the gas pressure at the second peak under the CVC exceeds its counterpart under the CCC by almost 1 MPa, see the red
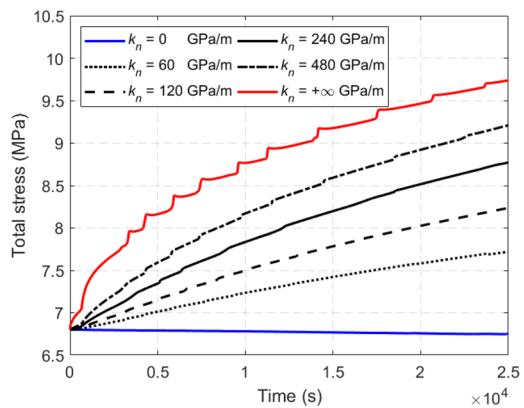
Fig. 13 Evolutions of water pressure, vertical displacement and total stress under different boundary conditions
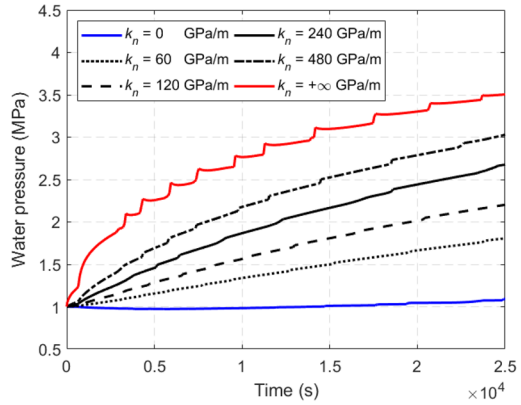
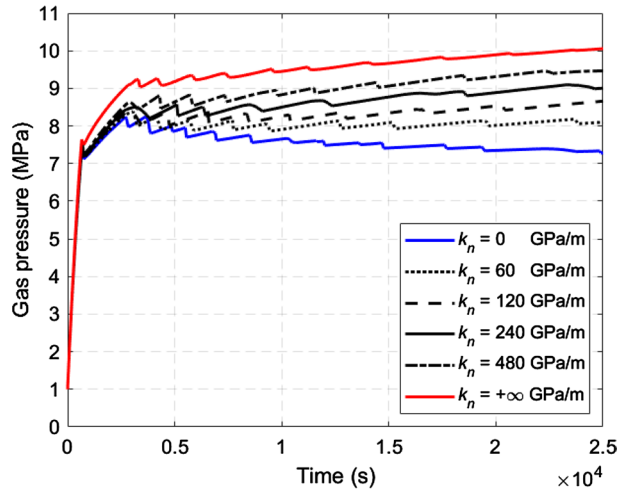**(a)** Water pressure at monitoring point A
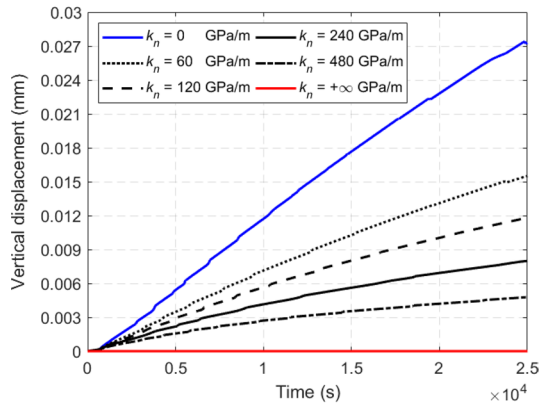
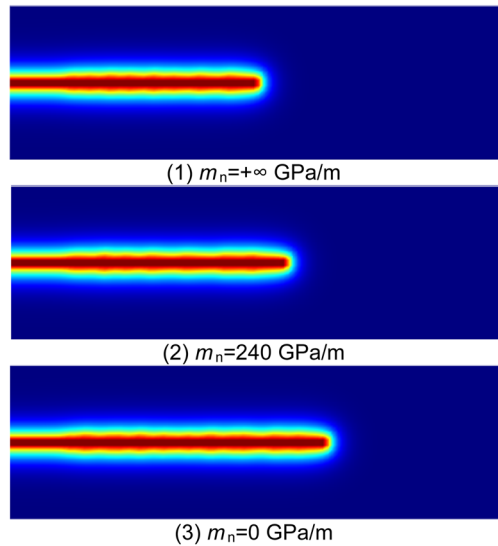**(b)** Vertical displacement at monitoring point A

(c) Total stress at monitoring point A

Fig. 14 Evolution of gas pressure and profiles of phase field under different boundary conditions

(a) Evolutions of gas pressure at the injection zone

(1) $m_n = +\infty$ GPa/m

(2) $m_n = 240$ GPa/m

(3) $m_n = 0$ GPa/m

(b) Profiles of phase field at time $v = 20000$s

and blue lines in Fig. 14a. This difference essentially results from the restraint of the rigid boundary, as previously discussed. This is qualitatively consistent with the experimental finding in Graham et al. (2012), Harrington and Horseman (2003) that shows the gas pressure for the breakthrough phenomenon is higher for the CVC than that for the CCC. In addition, after the second peak, the gas pressure under CVC experiences an increasing trend, while the pressure under CCC shows a decreasing trend. This is essentially caused by the different rates of fracture propagation controlled by the boundary stiffness. With the increase of the normal stiffness, the capability of the spring to restrain the dilation of the domain is enhanced. In other words, at a given dilation amount, the spring with larger

normal stiffness provides a larger compressive load to the domain. Therefore, the fracture propagation is more difficult to take place under the boundary condition with a higher stiffness. This is reflected in Fig. 14b where the length of the developed fracture is smaller for the case of higher stiffness at a specific moment. As analyzed above, the fracture propagates more rapidly under the CCC, see Fig. 14b3, than that under the CVC, see Fig. 14b1. If the rate of fracture propagation is large enough to counteract the rate of gas injection, the gas pressure will present a decreasing trend, see the blue line in Fig. 14a. Otherwise, the gas pressure experiences an increasing trend, see the red line in Fig. 14 (a).

As analyzed above, the numerical results are qualitatively consistent with the experimental results as discussed in Graham et al. (2012), Daniels and Harrington (2017), Harrington and Horseman (2003). Therefore, the proposed coupled HM-PF model can well describe the evolutions of the fluid pressure, the displacement and the total stress under different boundary conditions.

### 6.2.3 Hydromechanical Behaviors Under CVC

Previous experimental studies were mainly conducted under the CVC, since the boundary condition is close to the condition in the field. Therefore, the hydromechanical behaviors of the sample under the CVC will be analyzed in detail in this section.

Figure 15 presents the profiles of the degree of saturation and the distribution of gas pressure at time $t = 20000$ s. The profile of the degree of saturation is similar to that of the phase field, as compared between Figs. 14b1 and 15a. The degree of saturation in the developed fracture is close to zero, while the remaining of the domain is almost fully saturated. This result is qualitatively consistent with the experimental finding that concluded

(a) Profile of degree of saturation   **(b)** Distribution of gas pressure
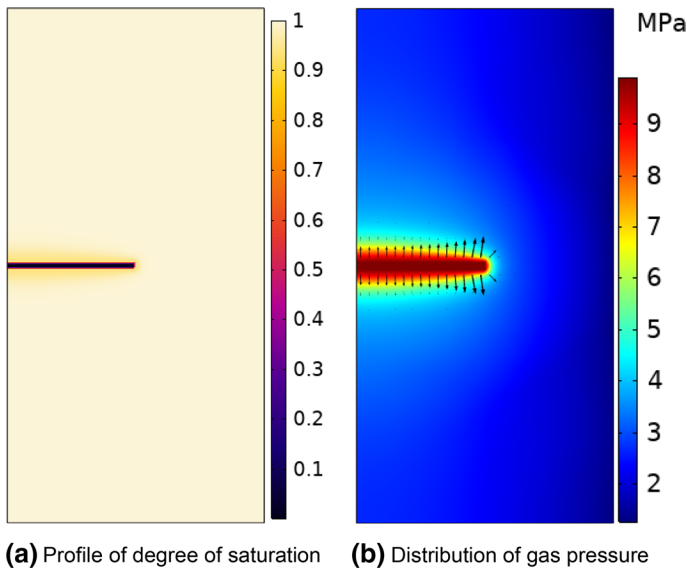
Fig. 15 Profiles of degree of saturation and distribution of gas pressure at time $t = 20000$ s (*Note*: Black arrows in the figure represent the gas flux. The length of the arrow is proportional to the magnitude of the flux)

Fig. 16 Distributions of water pressure and volumetric strain at time $t\,s = 20000$ s

(a) Distribution of water pressure

(b) Water pressure and volumetric strain along the cut line A-B
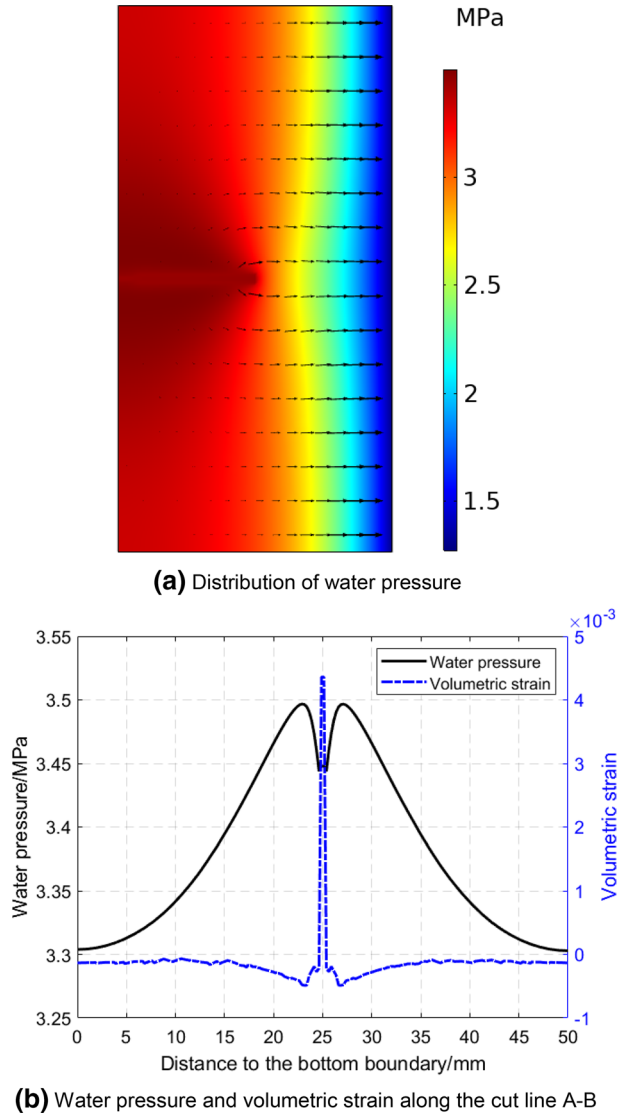
that the sample can remain in an almost saturated state after the gas injection test (Graham et al. 2012; Horseman et al. 1999; Harrington et al. 2017; Harrington and Horseman 2003). Corresponding to the distribution of the degree of saturation, the high gas pressure is localized around the developed fracture, as seen in Fig. 15b. As the gas entry value in the intact porous media is very high, i.e., 18 MPa, the area adjacent to the fracture is slightly desaturated, see Fig. 15a. According to the power law model, i.e., Eq. (61), the relative permeability of gas is very low when the effective degree of saturation is over 0.8, as seen in Fig. 3. Therefore, the highly pressurized gas can hardly transport from the fracture to the surrounding porous matrix, thus leading to a preferential gas flow in the developed fracture. On the other hand, the primary gas transport within the simulated domain mainly occurs around the developed fracture, as shown by the black arrows in Fig. 15b, since the

pressure gradient is larger there compared with other parts of the domain. In general, the developed coupled HM model has qualitatively captured the preferential gas flow which is commonly observed in experiments (Graham et al. 2012; Harrington et al. 2017, 2019).

Figure 16a presents the distribution of water pressure within the simulated domain at time $t = 20000$ s. The water pressure in the porous matrix at the two sides of the developed fracture has significantly built up. This is caused by the compressive load exerted by the highly pressurized gas. As the CVC does not allow any dilations, the porewater in the porous matrix is significantly compressed, thus leading to the increase of porewater pressure. As seen in Fig. 16a, the water pressure and the volumetric strain along the cut line A-B, as marked in Fig. 6, are presented. At the center of the line where the fracture is located, the porous media is subjected to a significant tensile volumetric strain due to the high gas pressure, see the blue dashed line in Fig. 16b. As the distance to the fracture increases, the volumetric strain rapidly drops to a negative value (i.e., compressive strain), forming two minimum values besides the fracture. This means the porous matrix adjacent to the developed fracture has experienced a consolidation process during the fracturing period. This numerical result is consistent with the statement in Graham et al. (2012), Harrington et al. (2017) that the generation of microfractures can result in a localized consolidation. As the distance to the fracture further increases, the volumetric strain gradually increases, but it remains less than zero. Corresponding to the evolution of volumetric strain along the cut line A-B, the water pressure reaches a maximum value beside the developed fracture and then gradually decreases with the increase of the distance to the fracture. This numerical result indicates that the water pressure is closely associated with the volumetric strain. Due to the build-up of the water pressure along the developed fracture, the water flows out of the sample under the formed pressure gradient. However, it is worth noting that the sample, except for the fracture zone, is still in an almost full saturation, as seen in Fig. 15a, due to the low intrinsic permeability and the high gas entry value in the porous matrix.

As analyzed above, some key experimental findings, such as the preferential gas flow, the build-up of porewater pressure, the almost fully saturated state after the gas injection test and the localized consolidation, have been qualitatively captured by the developed coupled HM-PF model.

7 Conclusions

A coupled HM-PF model is rigorously developed in this paper based on Coussy's thermodynamic theory for unsaturated soils and the microforce balance law. The possible contribution of interfaces between different phases to the fracturing process has been accounted for in the proposed framework. Specifically, the free energy of the interfaces has been analytically included in the effective stress tensor and the fracture driving force functional for the phase field model. However, due to the limited experimental studies, the effect of interfaces on the fracturing process has not been considered when simulating the gas-driven fracturing process in saturated bentonite.

The swelling pressure is an important factor controlling the gas entry into the saturated bentonite. In this paper, the swelling pressure is regarded as an initial stress. A fictitious strain tensor is calculated from this initial stress tensor based on the linear elastic theory. A modified strain tensor, which is used to construct the phase field model, is obtained by adding the fictitious strain tensor to the strain tensor due to deformation. The validation

simulations showed that the proposed HM-PF model can satisfactorily capture the effect of initial stress state on the fracturing process. Specifically, both the GFC and the RFC can be used to describe the fracturing under the isotropic initial stress state, while the RFC is more appropriate than the GFC to govern the fracturing process under the anisotropic initial stress state. In addition, the proposed coupled HM-PF model is able to qualitatively reproduce some of the experimental behaviors during gas migration in saturation bentonite. For example, the gas pressure required for triggering the fracturing process in bentonite should exceed the sum of the swelling pressure and the porewater pressure. Due to the strong constraint of the CVC, the gas pressure in the developed fracture, and the water pressure in porous matrix are higher than those under the CCC. In addition, the preferential gas flow, the build-up of porewater pressure, the almost fully saturated state and the localized consolidation have also been captured by the proposed model.

This paper mainly focuses on the thermodynamic consistence of the coupled HM-PF model and the effect of initial stress state on the fracturing process. The other commonly observed behaviors in experiment, such as the gas breakthrough phenomenon, the "shut-in" pressure and the fracture self-healing process, have not yet been captured by the proposed model. To reproduce these experimentally observed behaviors may need more advanced permeability model and mechanical model that can describe both the damaging and healing process. These works may be left for future studies.

Code Availability All models and code generated or used during the study appear in the submitted article.

Compliance with Ethical Standards

Conflict of interest There are no potential conflicts of interests and competing interests.

Availability of Data and Material All data, models, materials and code generated or used during the study appear in the submitted article.

References

Achanta, S., Cushman, J.H., Okos, M.R.: On multicomponent, multiphase thermomechanics with interfaces. Int. J. Eng. Sci. **32**(11), 1717–1738 (1994)

Alonso, E.E., Vaunat, J., Gens, A.: Modelling the mechanical behaviour of expansive clays. Eng. Geol. **54**(1–2), 173–183 (1999)

Amarasiri, A.L., Kodikara, J.K.: Numerical modeling of desiccation cracking using the cohesive crack method. Int. J. Geomech. **13**(3), 213–221 (2011)

Arnedo, D., Alonso, E.E., Olivella, S.: Gas flow in anisotropic claystone: modelling triaxial experiments. Int. J. Numer. Anal. Methods. Geomech. **37**(14), 2239–2256 (2013)

Bennethum, L.S., Murad, M.A., Cushman, J.H.: Modified Darcy's law, Terzaghi's effective stress principle and Fick's law for swelling clay soils. Comput. Geotech. **20**(3–4), 245–266 (1997)

Borja, R.I.: On the mechanical energy and effective stress in saturated and unsaturated porous continua. Int. J Solids Struct. **43**(6), 1764–1786 (2006)

Borja, R.I., Koliji, A.: On the effective stress in unsaturated porous continua with double porosity. J. Mech. Phys. Solids **57**(8), 1182–1193 (2009)

Bourdin, B., Francfort, G.A., Marigo, J.J.: Numerical experiments in revisited brittle fracture. J. Mech. Phys. Solids **48**(4), 797–826 (2000)

Cajuhi, T., Sanavia, L., De Lorenzis, L.: Phase-field modeling of fracture in variably saturated porous media. Comput. Mech. **61**, 299–318 (2018)

Carrier, B., Granet, S.: Numerical modeling of hydraulic fracture problem in permeable medium using cohesive zone model. Eng. Fract. Mech. **79**, 312–328 (2012)

Chapuis, R.P., Aubertin, M.: On the use of the Kozeny Carman equation to predict the hydraulic conductivity of soils. Can. Geotech. J. **40**(3), 616–628 (2003)

Chen, B., Sun, Y., Barboza, B.R., Barron, A.R., Li, C.: Phase-field simulation of hydraulic fracturing with a revised fluid model and hybrid solver. Eng. Fract. Mech. **229**, 106928 (2020)

Choo, J., Borja, R.I.: Stabilized mixed finite elements for deformable porous media with double porosity. Comput. Method Appl. Mater **293**, 131–154 (2015)

Choo, J., Sun, W.: Cracking and damage from crystallization in pores: coupled chemo-hydro-mechanics and phase-field modeling. Comput. Method Appl. Mater. **335**, 347–379 (2018)

Choo, J., Sun, W.: Coupled phase-field and plasticity modeling of geological materials: from brittle fracture to ductile flow. Comput Method Appl M **330**, 1–32 (2018a)

Choo, J., Sun, W.: Cracking and damage from crystallization in pores: coupled chemo-hydro-mechanics and phase-field modeling. Comput. Method Appl. Mater. **335**, 47–379 (2018b)

Choo, J., White, J.A., Borja, R.I.: Hydromechanical modeling of unsaturated flow in double porosity media. Int. J. Geomech. **16**(6), D4016002 (2016)

Coussy, O.: Poromechanics. Wiley, New York (2004)

Coussy, O.: Revisiting the constitutive equations of unsaturated porous solids using a Lagrangian saturation concept. Int. J. Numer. Anal. Methods Geomech. **31**(15), 1675–1694 (2007)

Cueto-Felgueroso, L., Juanes, R.: A phase-field model of two-phase Hele–Shaw flow. J. Fluid Mech. **758**, 522–552 (2014)

Cuss, R.J., Harrington, J.F., Noy, D.J., Graham, C.C., Sellin, P.: Evidence of localised gas propagation pathways in a field-scale bentonite engineered barrier system; results from three gas injection tests in the large scale gas injection test (Lasgit). Appl Clay Sci **102**, 81–92 (2014)

Dagher, E., Nguyen, T., Sedano, J.I.: Development of a mathematical model for gas migration (two-phase flow) in natural and engineered barriers for radioactive waste disposal. Geol. Soc. Lond. Spec. Publ. **482**(SP482), 14 (2018)

Daniels, K.A., Harrington, J.: The response of compact bentonite during a 1-D gas flow test. British Geological Survey. OR/17/067 (2017)

De Lorenzis, L., McBride, A., Reddy, B.: Phase-field modelling of fracture in single crystal plasticity. GAMM-Mitteilungen **39**(1), 7–34 (2016)

Doughty, C.: Modeling geologic storage of carbon dioxide: comparison of non-hysteretic and hysteretic characteristic curves. Energy Convers. Manage **48**(6), 1768–1781 (2007)

Espinoza, D.N., Santamarina, J.C.: Clay interaction with liquid and supercritical CO_2: the relevance of electrical and capillary forces. Int J Greenh Gas Con **10**, 351–362 (2012)

Fall, M., Nasir, O., Nguyen, T.S.: A coupled hydro-mechanical model for simulation of gas migration in host sedimentary rocks for nuclear waste repositories. Eng. Geol. **176**, 24–44 (2014)

Fourar, M., Lenormand, R.: A viscous coupling model for relative permeabilities in fractures. In: SPE Annual Technical Conference and Exhibition. Society of Petroleum Engineers (1998)

Gens, A., Alonso, E.E.: A framework for the behavior of unsaturated expansive clays. Can. Geotech. J. **29**(6), 1013–1032 (1992)

Gens Solé, A., Vállejan, B., Sánchez, M., Imbert, C., Villar, M.V., Van Geetl, M.: Hydromechanical behaviour of a heterogeneous compacted soil: experimental observations and modelling. Géotechnique **61**(5), 367–386 (2011)

Gerard, P., Harrington, J., Charlier, R., Collin, F.: Modelling of localised gas preferential pathways in claystone. Int. J. Rock Mech. Min. Sci. **67**, 104–114 (2014)

Graham, C.C., Harrington, J.F., Cuss, R.J., Sellin, P.: Gas migration experiments in bentonite: implications for numerical modelling. Min. Mag. **76**(8), 3279–3292 (2012)

Graham, C.C., Harrington, J.F., Sellin, P.: Gas migration in pre-compacted bentonite under elevated porewater pressure conditions. Appl. Clay Sci. **132–133**, 353–365 (2016)

Gui, Y., Hu, W., Zhao, Z., Zhu, X.: Numerical modelling of a field soil desiccation test using a cohesive fracture model with Voronoi tessellations. Acta Geotech. **13**, 87–102 (2017)

Guo, G., Fall, M.: Modelling of dilatancy-controlled gas flow in saturated bentonite with double porosity and double effective stress concepts. Eng. Geol. **243**, 253–271 (2018)

Guo, G., Fall, M.: Modelling of preferential gas flow in heterogeneous and saturated bentonite based on phase field method. Comput. Geotech. **116**, 103206 (2019)

Guo, G., Fall, M.: A double pore structure model for gas migration in saturated bentonite accounting for damaging effects and hysteresis of permeability, submitted for publication (2020)

Gurtin, M.E.: Generalized Ginzburg–Landau and Cahn–Hilliard equations based on a microforce balance. Phys. D **92**(3), 178–192 (1996)

Harrington, J.,Horseman, S.: Gas migration in KBS-3 buffer bentonite, Sensitivity of Test Parameters to Experimental Boundary ConditionsSwedish Nuclear Fuel and Waste Management Company, Stockholm (Sweden) (2003)

Harrington, J., Milodowski, A., Graham, C., Rushton, J., Cuss, R.: Evidence for gas-induced pathways in clay using a nanoparticle injection technique. Min. Mag **76**(8), 3327–3336 (2012)

Harrington, J.F., Graham, C.C., Cuss, R.J., Norris, S.: Gas network development in a precompacted bentonite experiment: evidence of generation and evolution. Appl. Clay Sci. **147**, 80–89 (2017)

Harrington, J., Graham, C., Cuss, R., Norris, S.: Gas network development in compact bentonite: key controls on the stability of flow pathways. Geofluids **2019**, 1–19 (2019)

Heider, Y., Sun, W.: A phase field framework for capillary-induced fracture in unsaturated porous media: drying-induced vs. hydraulic cracking. Comput. Method Appl. Mater. **359**, 112647 (2020)

Horseman, S.T., Harrington, J.F., Sellin, P.: Gas migration in clay barriers. Eng. Geol. **54**(1–2), 139–149 (1999)

Jain, A., Juanes, R.: Preferential mode of gas invasion in sediments: grain-scale mechanistic model of coupled multiphase fluid flow and sediment mechanics. J. Geophys. Res. Solid Earth **114**(B8), 1–19 (2009)

Juanes, R., Spiteri, E., Orr, F., Blunt, M.: Impact of relative permeability hysteresis on geological CO_2 storage. Water Resour. Res. **42**(12), 1–13 (2006)

Killough, J.: Reservoir simulation with history-dependent saturation functions. Soc. Petrol. Eng. J. **16**(01), 37–48 (1976)

Lee, S., Wheeler, M.F., Wick, T.: Pressure and fluid-driven fracture propagation in porous media using an adaptive finite element phase field model. Comput. Method Appl. Mater. **305**, 111–132 (2016)

Lenhard, R., Parker, J.: A model for hysteretic constitutive relations governing multiphase flow: 2. Permeability-saturation relations. Water Resour. Res. **23**(12), 2197–2206 (1987)

Li, W., Wei, C.: Stabilized low-order finite elements for strongly coupled poromechanical problems. Int. J. Numer. Methods Eng. **115**(5), 531–548 (2018)

Liu, J.F., Skoczylas, F., Talandier, J.: Gas permeability of a compacted bentonite-sand mixture: coupled effects of water content, dry density, and confining pressure. Can. Geotech. J. **52**(8), 1159–1167 (2015)

Liu, J.-F., Song, Y., Skoczylas, F., Liu, J.: Gas migration through water-saturated bentonite–sand mixtures, COx argillite, and their interfaces. Can. Geotech. J. **53**(1), 60–71 (2016)

Luckner, L., Vangenuchten, M.T., Nielsen, D.R.: A consistent set of parametric models for the 2-phase flow of immiscible fluids in the subsurface. Water Resour. Res. **25**(10), 2187–2193 (1989)

Mahjoub, M., Rouabhi, A., Tijani, M., Granet, S., M'jahad, S., Talandier, J. : Numerical study of Callovo-Oxfordian argillite expansion due to gas injection. Int. J. Geomech. **18**(1), 04017134 (2017)

Marschall, P., Horseman, S., Gimmi, T.: Characterisation of gas transport properties of the Opalinus Clay, a potential host rock formation for radioactive waste disposal. Oil Gas Sci. Technol. **60**(1), 121–139 (2005)

Mauthe, S., Miehe, C.: Hydraulic fracture in poro-hydro-elastic media. Mech. Res. Commun. **80**, 69–83 (2017)

Miehe, C., Mauthe, S.: Phase field modeling of fracture in multi-physics problems. Part III. Crack driving forces in hydro-poro-elasticity and hydraulic fracturing of fluid-saturated porous media. Comput. Method Appl. Mater. **304**, 619–655 (2016)

Miehe, C., Welschinger, F., Hofacker, M.: Thermodynamically consistent phase-field models of fracture: variational principles and multi-field FE implementations. Int. J. Numer. Methods Eng. **83**(10), 1273–1311 (2010a)

Miehe, C., Hofacker, M., Welschinger, F.: A phase field model for rate-independent crack propagation: robust algorithmic implementation based on operator splits. Comput. Method Appl. Mater. **199**(45–48), 2765–2778 (2010b)

Miehe, C., Schänzel, L.-M., Ulmer, H.: Phase field modeling of fracture in multi-physics problems. Part I. Balance of crack surface and failure criteria for brittle crack propagation in thermo-elastic solids. Comput. Method Appl. Mater. **294**, 449–485 (2015)

Mikelić, A., Wheeler, M.F., Wick, T.: Phase-field modeling of a fluid-driven fracture in a poroelastic medium. Comput. Geosci. **19**(6), 1171–1195 (2015)

Mohammadnejad, T., Khoei, A.: Hydro-mechanical modeling of cohesive crack propagation in multiphase porous media using the extended finite element method. Int. J. Numer. Anal. Meth. Geomech. **37**(10), 1247–1279 (2013a)

Mohammadnejad, T., Khoei, A.: An extended finite element method for hydraulic fracture propagation in deformable porous media with the cohesive crack model. Finite Elem. Anal. Des. **73**, 77–95 (2013b)

Mualem, Y.: A new model for predicting the hydraulic conductivity of unsaturated porous media. Water Resour. Res. **12**(3), 513–522 (1976)

Na, S., Sun, W.: Computational thermomechanics of crystalline rock, Part I: a combined multi-phase-field/crystal plasticity approach for single crystal simulations. Comput. Method Appl. Mater. **338**, 657–691 (2018)

Nguyen, T., Le, A.: Simultaneous gas and water flow in a damage-susceptible bedded argillaceous rock. Can. Geotech. J. **52**(1), 18–32 (2014)

Nguyen, V.P., Lian, H., Rabczuk, T., Bordas, S.: Modelling hydraulic fractures in porous media using flow cohesive interface elements. Eng. Geol. **225**(8), 68–82 (2017)

Olivella, S., Alonso, E.E.: Gas flow through clay barriers. Geotechnique **58**(3), 157–176 (2008)

Parker, J., Lenhard, R.: A model for hysteretic constitutive relations governing multiphase flow: 1. Saturation-pressure relations. Water Resour. Res. **23**(12), 2187–2196 (1987)

Qi, S., Vanapalli, S.K.: Simulating hydraulic and mechanical responses of unsaturated expansive soil slope to rainfall: Case Study. Int. J. Geomech. **18**(6), 05018002 (2018)

Rodwell, W.R., Harris, A.W., Horseman, S.T., Lalieux, P., Muller, W., Amaya, L.O.,Pruess, K.: Gas migration and twophase flow through engineered and geological barriers for a deep repository for radioactive waste. Nuclear Energy Agency (1999)

Salimzadeh, S., Khalili, N.: A three-phase XFEM model for hydraulic fracturing with cohesive crack propagation. Comput. Geotech. **69**, 82–92 (2015)

Sánchez, M., Gens, A., Villar, M.V., Olivella, S.: Fully coupled thermo-hydro-mechanical double-porosity formulation for unsaturated soils. Int. J. Geomech. **16**(6), D4016015 (2016)

Santillán, D., Juanes, R., Cueto-Felgueroso, L.: Phase field model of fluid-driven fracture in elastic media: immersed-fracture formulation and validation with analytical solutions. J. Geophys. Res. Solid Earth **122**(4), 2565–2589 (2017)

Santillán, D., Juanes, R., Cueto-Felgueroso, L.: Phase-field model of hydraulic fracturing in poroelastic media: fracture propagation, arrest and branching under fluid injection and extraction. J. Geophys. Res. Solid Earth **123**(3), 2127–2155 (2018)

Shin, H., Santamarina, J.: Desiccation cracks in saturated fine-grained soils: particle-level phenomena and effective-stress analysis. Géotechnique **61**(11), 961 (2011)

Snow, D.T.: Anisotropie permeability of fractured media. Water Resour. Res. **5**(6), 1273–1289 (1969)

Song, X., Ye, M., Wang, K.: Strain localization in a solid-water-air system with random heterogeneity via stabilized mixed finite elements. Int. J. Numer. Methods Eng. **112**(13), 1926–1950 (2017)

Spiteri, E.J., Juanes, R.: Impact of relative permeability hysteresis on the numerical simulation of WAG injection. J. Petrol. Sci. Eng. **50**(2), 115–139 (2006)

Tamayo-Mas, E., Harrington, J., Shao, H., Dagher, E., Lee, J., Kim, K., Rutqvist, J., Lai, S., Chittenden, N., Wang, Y.: Numerical modelling of gas flow in a compact clay barrier for DECOVALEX-2019. In: Proceeding of the 2nd international discrete fracture network engineering conference, Seattle,Washington, USA, 20–22 June 2018, pp ARMA-DFNE-18-0623. ARMA (2018)

Taron, J., Elsworth, D.: Thermal–hydrologic–mechanical–chemical processes in the evolution of engineered geothermal reservoirs. Int. J. Rock Mech. Min. Sci. **46**(5), 855–864 (2009)

Taron, J., Elsworth, D., Min, K.-B.: Numerical simulation of thermal-hydrologic-mechanical-chemical processes in deformable, fractured porous media. Int. J. Rock Mech. Min. Sci. **46**(5), 842–854 (2009)

van Genuchten, M.T.: A closed-form equation for predicting the hydraulic conductivity of unsaturated soils. Soil Sci. Soc. Am. J. **44**(5), 892–898 (1980)

Wang, J.J., Zhu, J.G., Chiu, C.F., Zhang, H.: Experimental study on fracture toughness and tensile strength of a clay. Eng. Geol. **94**(1–2), 65–75 (2007)

Wheeler, M.F., Wick, T., Lee, S.: IPACS: integrated phase-field advanced crack propagation simulator. An adaptive, parallel, physics-based-discretization phase-field framework for fracture propagation in porous media. Comput. Method Appl. Mater. **367**, 113124 (2020)

White, J.A., Borja, R.I.: Stabilized low-order finite elements for coupled solid-deformation/fluid-diffusion and their application to fault zone transients. Comput. Method Appl. Mater. **197**(49–50), 4353–4366 (2008)

Wilson, Z.A., Borden, M.J., Landis, C.M.: A phase-field model for fracture in piezoelectric ceramics. Int. J. Fract. **183**(2), 135–153 (2013)

Wiseall, A., Cuss, R., Graham, C., Harrington, J.: The visualization of flow paths in experimental studies of clay-rich materials. Min. Mag. **79**(6), 1335–1342 (2015)

Xu, W.J., Shao, H., Hesser, J., Wang, W., Schuster, K., Kolditz, O.: Coupled multiphase flow and elasto-plastic modelling of in-situ gas injection experiments in saturated claystone (Mont Terri Rock Laboratory). Eng. Geol. **157**, 55–68 (2013)

Xu, L., Ye, W.M., Ye, B., Chen, B., Chen, Y.G., Cui, Y.J.: Investigation on gas migration in saturated materials with low permeability. Eng. Geol. **197**, 94–102 (2015)

Xu, L., Ye, W.M., Chen, B., Chen, Y.G., Cui, Y.J.: Experimental investigations on thermo-hydro-mechanical properties of compacted GMZ01 bentonite-sand mixture using as buffer materials. Eng. Geol. **213**, 46–54 (2016)

Xu, L., Ye, W., Chen, Y., Chen, B., Cui, Y.: A new approach for determination of gas breakthrough in saturated materials with low permeability. Eng. Geol. **241**, 121–131 (2018)

Ye, W.M., Xu, L., Chen, B., Chen, Y.G., Ye, B., Cui, Y.J.: An approach based on two-phase flow phenomenon for modeling gas migration in saturated compacted bentonite. Eng. Geol. **169**, 124–132 (2014)

Yin, P., Vanapalli, S.K.: Model for predicting tensile strength of unsaturated cohesionless soils. Can. Geotech. J. **55**(9), 1313–1333 (2018)

Zheng, L., Rutqvist, J., Xu, H., Kim, K., Voltolini, M., Cao, X.: Investigation of coupled processes and impact of high temperature limits in argillite rock: FY17 Progress. Ernest Orlando Lawrence Berkeley National Laboratory, Berkeley, CA (2017)

Zhou, S., Zhuang, X., Rabczuk, T.: A phase-field modeling approach of fracture propagation in poroelastic media. Eng. Geol. **240**, 189–203 (2018)

Zhou, S., Zhuang, X., Rabczuk, T.: Phase field method for quasi-static hydro-fracture in porous media under stress boundary condition considering the effect of initial stress field. Theor. Appl. Fract. Mech. **107**, 102523 (2020)